

# The spectra of IceCube Neutrino (SIN) candidate sources - III. Optical spectroscopy and source characterization of the full sample

Simona Paiano<sup>1,2\*</sup>, Renato Falomo<sup>3</sup>, Aldo Treves<sup>4,5</sup>, Paolo Padovani<sup>6,7</sup>,  
Paolo Giommi<sup>8,9,10</sup>, Riccardo Scarpa<sup>11,12</sup>, Susanna Bisogni<sup>2</sup>, Ester Marini<sup>13</sup>

<sup>1</sup>INAF - IASF Palermo, via Ugo La Malfa, 153, I-90146, Palermo, Italy

<sup>2</sup>INAF - IASF Milano, via Corti 12, I-20133, Milano, Italy

<sup>3</sup>INAF - Osservatorio Astronomico di Padova, vicolo dell'Osservatorio 5, I-35122, Padova, Italy

<sup>4</sup>Università dell'Insubria, via Valleggio, 22100, Como, Italy

<sup>5</sup>INAF - Osservatorio Astronomico di Brera, via Bianchi 46, I-23807, Merate (Lecco), Italy

<sup>6</sup>European Southern Observatory, Karl-Schwarzschild-Str. 2, D-85748 Garching bei München, Germany

<sup>7</sup>Associated to INAF - Osservatorio di Astrofisica e Scienza dello Spazio, Via Piero Gobetti 93/3, I-40129 Bologna, Italy

<sup>8</sup>Institute for Advanced Study, Technische Universität München, Lichtenbergstrasse 2a, D-85748 Garching bei München, Germany

<sup>9</sup>Center for Astro, Particle and Planetary Physics (CAP3), New York University Abu Dhabi, PO Box 129188 Abu Dhabi, United Arab Emirates

<sup>10</sup>Associated to Agenzia Spaziale Italiana, ASI, via del Politecnico s.n.c., I-00133 Roma Italy

<sup>11</sup>Instituto de Astrofísica de Canarias, C/O Via Lactea, s/n E38205 - La Laguna (Tenerife) - Spain

<sup>12</sup>Universidad de La Laguna, Dpto. Astrofísica, s/n E-38206 La Laguna (Tenerife) - Spain

<sup>13</sup>INAF - Osservatorio Astronomico di Roma, via Frascati 33, I-00077 Monte Porzio Catone (RM), Italy

Received : ; Accepted :

## ABSTRACT

A correlation between astrophysical high-energy neutrinos and blazars has been suggested by various authors. In particular, a likely association between IceCube events and intermediate and high-energy peaked BL Lac objects has led to a sample of 47 objects having a high probability of being neutrino sources. In the first paper of this series we reported optical spectroscopy of 17 objects, which together with data taken from the literature covered 80 per cent of the sample. Here we present spectroscopy obtained at large aperture telescopes of a further 17 objects (plus four additional targets), which completes the sample coverage. For twelve objects we are able to determine the redshift ( $0.07 < z < 1.6$ ), while for the others we set a lower limit on it, based on either the robust detection of intervening absorption systems or on an estimation derived from the absence of spectral signatures of the host galaxy. With these new data we expand and reinforce the main results of our previous papers, namely the fact that in terms of their broad-band properties our sources appear to be indistinguishable from the rest of the blazar population and the relatively large ( $> 34$  per cent and possibly as high as 80 per cent) fraction of *masquerading* BL Lac objects, for which the low equivalent width of the emission lines is due to the brightness of the boosted continuum, rather than being an intrinsic property, in our sample.

**Key words:** galaxies: active and redshifts — BL Lacertae objects: general — gamma-rays: galaxies — neutrino

## 1 INTRODUCTION

High-energy (TeV-PeV) neutrino astrophysics was born recently thanks to IceCube (IceCube Collaboration 2013). The quasi-isotropy of the distribution of neutrino events in the sky indicates a dominant component of extragalactic objects, which are also most probably linked to the sources of high energy cosmic rays (e.g. Resconi et al. 2017; Kurahashi, Murase, & Santander 2022).

Many authors (e.g. Righi, Tavecchio, & Inoue 2019; Giommi et al. 2020; Plavin et al. 2021; Hovatta et al. 2021; Buson et al. 2022, and references therein) have suggested a correlation between IceCube neutrinos and blazars, i.e. active galactic nuclei whose emission is dominated by a relativistic jet pointing towards the observer.

In particular, Giommi et al. (2020) (hereafter G20) considered all the 70 IceCube neutrino tracks known in 2020 and found a  $3.2\sigma$  post-trial correlation with intermediate- and high-energy (IBL and HBL)<sup>1</sup> blazars, i.e. objects where the synchrotron peak frequency is  $> 10^{14}$  Hz. Specifically, 30 neutrino events with well defined positions were matched with a set of 47 blazars (see Table 5 of G20), with  $16 \pm 4$  of those possibly being neutrino sources.

In order to test this scenario out, optical spectra are required, since

<sup>1</sup> Based on the rest-frame frequency of the low-energy synchrotron peak ( $\nu_{\text{peak}}^S$ ), blazars are divided into low- (LBL:  $\nu_{\text{peak}}^S < 10^{14}$  Hz [ $< 0.41$  eV]), intermediate- (IBL:  $10^{14}$  Hz  $< \nu_{\text{peak}}^S < 10^{15}$  Hz [ $0.41 - 4.1$  eV]), and high-energy (HBL:  $\nu_{\text{peak}}^S > 10^{15}$  Hz [ $> 4.1$  eV]) peaked objects respectively (Padovani et al. 1995; Abdo et al. 2010).

\* E-mail: simona.paiano@inaf.it

the majority of the G20 sample did not have redshift determinations. These are obviously needed to derive the luminosity of the source, vital for any modelling, determine the properties of the spectral lines, and also possibly estimate the mass of the central black hole,  $M_{\text{BH}}$ . Our group has therefore started “The spectra of IceCube Neutrino (SIN) candidate sources” project, which has so far led to two papers. In the first paper (Paiano et al. 2021; hereafter Paper I) we obtained optical spectroscopy of 17 of the G20 sources, which together with spectra gathered from the literature, covered  $\sim 80$  per cent of the G20 sources. All objects but one (a quasar), were shown to be BL Lac objects (BLLs): the redshift was measured for half of them, and for the rest a lower limit was given.

In the second paper (Padovani et al. 2022; hereafter Paper II) it was shown that the BLLs under scrutiny were in many cases (40 – 80 per cent) masquerading BLLs, i.e. objects where the weakness of the emission lines and their low values of the Equivalent Width (EW) is due to a very bright Doppler boosted continuum, which is washing out the lines. Note that TXS 0506+056, which is the blazar with the most significant association with neutrino events (IceCube Collaboration et al. 2018a,b; Baikal-GVD Collaboration et al. 2022) is also a masquerading BLL (Padovani et al. 2019). Paper II discussed also in some details possible jet models for high-energy neutrino production.

We report here on optical spectroscopy of 17 targets, plus other four sources (referred to as “extra”) associated to neutrino events posterior to G20. This completes the spectroscopy coverage for the G20 sample. The spectra were taken at large diameter telescopes, i.e. the Gran Telescopio Canarias (GTC), the Very Large Telescope (VLT), and the Large Binocular Telescope (LBT).

This paper is organized as follows: in Section 2 we present the sample, in Section 3 we describe the data and their reduction. In Section 4 we present the observational results, the main properties of the features found in the spectra and discuss the redshift measurements. In Section 5 we give details on individual objects. In Section 6 we characterize the G20 sources, while Section 7 does that for the extra objects. Finally, Section 8 discusses our results and Section 9 summarises our conclusions. Appendix A shows flux calibrated and de-reddened spectra for our sources, some examples of close-ups around the detected spectral lines, and spectral decompositions of the observed optical spectra into a power-law and an elliptical template galaxy.

We use a  $\Lambda$ CDM cosmology with Hubble constant  $H_0 = 70 \text{ km s}^{-1} \text{ Mpc}^{-1}$ , matter density  $\Omega_{\text{m},0} = 0.3$ , and dark energy density  $\Omega_{\Lambda,0} = 0.7$ .

## 2 THE SAMPLE

In Paper I we considered a sample of 47  $\gamma$ -ray sources matched to 30 neutrino events with well-defined IceCube positions (area of the error ellipse smaller than that of a circle with radius  $r = 3^\circ$ ) and we presented spectroscopic data for 17 objects of them with previously unknown or uncertain redshift in the literature.

In this work we report on optical spectroscopy of further 21 sources (see Table 1) with unknown or uncertain redshift or with low quality optical spectrum with the aim of determining the distance and the main spectral properties. Among them, 17 sources belong to the original G20 sample while 4 objects (4FGL J0258.1+2030, 4FGL J0545.0+0613, 4FGL J0658.6+0636 and 4FGL J1702.2+2642) are newly added because they were proposed as potential counterparts of Icecube detections recorded after the publication of G20. Most of these sources satisfy all the G20

selection criteria ( $|b_{\text{II}}| > 10^\circ$ ,  $\nu_{\text{peak}}^S > 10^{14} \text{ Hz}$ , and area of the error ellipse), apart from 4FGL J0258.1+2030/IceCube-191231A, which violates the area constrain but represents a rare case of an object associated with more than one neutrino track, and 4FGL J0545.0+0613c whose spectral energy distribution (SED) is dominated by thermal emission and for which is therefore impossible to determine  $\nu_{\text{peak}}^S$ . More details are reported in the notes of the single sources in Section 5. A journal of the observations of the 21 sources is given in Table 2.

## 3 OBSERVATIONS AND DATA REDUCTION

The optical spectra were obtained using three different telescopes. Twelve sources located in the northern hemisphere were observed with the 10.4m GTC at the Roque de Los Muchachos (La Palma) equipped with the OSIRIS spectrograph (Cepa et al. 2003), configured with the grism R1000B (slit width of 1.2") that covers the spectral range 4100 – 7750 Å with a resolution  $R \sim 600$ . For 7 targets, the 8 m VLT-UT1 at Paranal using FORS2 (Appenzeller et al. 1998) was utilized. In this case, the grism GRIS\_300V+10 with slit width of 1.3" was used, sampling the range 4700 – 8500 Å with  $R \sim 200$ . Spectra of three sources were taken with the LBT, two twin 8.4m telescopes located in southeastern Arizona (Mt. Graham) using the MultiObject Double Spectrographs MODS-1 and MODS-2 (Pogge et al. 2010) in dual grating mode with the grisms G400L and G670L and a slit width of 1.2" and covering the spectral ranges 4000–9000 Å ( $R \sim 1000$ ).

Data reduction of the GTC observations was performed adopting standard IRAF procedures (Tody 1986, 1993) for long slit spectroscopy following the same scheme given in Paiano et al. (2017a). For FORS2 data we adopted the reduction pipeline provided by the EsoReflex environment (Freudling et al. 2013) including extraction of 1D spectra. Spectroscopy data reduction for LBT data was carried out at the Italian LBT Spectroscopic Reduction Center using the pipeline SIPGI (Gargiulo et al. 2022) and using the standard procedure for long-slit spectroscopy with bias subtraction, flat-fielding, and bad-pixel correction. In all cases the accuracy of the wavelength calibration based on the scatter of the polynomial fit (pixel vs wavelength) is  $\sim 0.1 \text{ Å}$  over the whole observed spectral range. In order to perform an optimal correction of cosmic rays and other artifacts, the observation of each source was divided in at least three individual exposures. This procedure allows us also to check for possible spurious features. The final spectrum results from the combination of all individual exposures.

Spectro-photometric standard stars were secured for each night in order to perform the relative flux calibration. In addition, we assessed the absolute flux calibration from the measured magnitude of the source (see Table 3) as derived from the acquisition images obtained during the observations. For each image we measured the observed magnitude of a number of stars in the SDSS and/or Pan-STARRS catalogues and derived the calibration constant of the frame, with an accuracy  $\sim 0.2$  magnitudes. A comparison with literature magnitudes (see Tab. 1) shows some variability in 4FGL J0658.6+0636 and 4FGL J1439.5–2525.

Finally all spectra were de-reddened applying the extinction law of Cardelli, Clayton & Mathis (1989) and assuming the value of Galactic extinction  $E(B-V)$  derived from the NASA/IPAC Infrared Science Archive<sup>2</sup> (Schlafly & Finkbeiner 2011).

<sup>2</sup> <http://irsa.ipac.caltech.edu/applications/DUST/>

**Table 1.** The sample of neutrino candidate blazars.

Object Name	Counterpart Name	IC event	Sep. (degrees)	RA (J2000)	DEC (J2000)	Mag. (g)	$\nu_{\text{peak}}^S$ (Hz)
4FGL J0258.1+2030	5BZB J0258+2030	IC-191231A/IC-211125A	2.11/2.08	02:58:07.3	+20:30:02.0	20.8	14.1
4FGL J0339.2-1736	3HSP J033913.7-173600	IC-141109A	1.24	03:39:14.7	-17:36:00.8	16.8	15.6
4FGL J0545.0+0613c	NVSS J054341+062553	IC-200421A	2.88	05:45:29.1	+06:19:58.0	21.3	...
4FGL J0658.6+0636	3HSP J065845.0+063711	IC-201114A	0.85	06:58:44.9	+06:37:11.5	18.9	15.5
4FGL J0946.2+0104	3HSP J094620.2+010451	IC-190819A	2.24	09:46:20.2	+01:04:51.6	20.0	>18.0
4FGL J1003.4+0205	3HSP J100326.6+020455	IC-190819A	2.35	10:03:26.6	+02:04:55.5	19.7	15.8
4FGL J1055.7-1807	VOU J105603-180929	IC-171015A	2.6	10:56:03.5	-18:09:30.2	20.5	14.1
4FGL J1124.0+2045	3HSP J112405.3+204553	IC-130408A	3.61	11:24:05.3	+20:45:52.9	18.8	15.3
4FGL J1124.9+2143	3HSP J112503.6+214300	IC-130408A	3.48	11:25:03.5	+21:43:04.0	18.5	15.8
4FGL J1314.7+2348	5BZB J1314+2348	IC-151017A	3.68	13:14:43.8	+23:48:26.6	17.1	$\geq 14$
4FGL J1321.9+3219	5BZB J1322+3216	IC-120515A	1.54	13:22:47.4	+32:16:08.7	19.3	14.5
4FGL J1439.5-2525	VOU J143934-252458	IC-170506A	1.81	14:39:34.6	-25:24:58.3	19.0	14.0
4FGL J1507.3-3710	VOU J150720-370902	IC-181014A	2.0	15:07:20.8	-37:09:02.8	17.5	14.5
4FGL J1528.4+2004	3HSP J152835.8+200420	IC-110521A	3.23	15:28:35.7	+20:04:20.2	20.2	16.2
4FGL J1702.2+2642	5BZB J1702+2643	IC-200530A	0.62	17:02:09.6	+26:43:15.0	18.5	13.9
4FGL J1808.2+3500	CRATES J180812+350104	IC-110610A	0.55	18:08:11.5	+35:01:18.8	15.4	14.5
4FGL J2030.9+1935	3HSP J203057.1+193612	IC-100710A	1.82	20:30:57.1	+19:36:12.8	18.6	15.8
4FGL J2030.5+2235	3HSP J203031.6+223439	IC-100710A	1.31	20:30:31.6	+22:34:39.3	20.3	16.2
4FGL J2133.1+2529c	3HSP J213314.3+252859	IC-150714A	2.18	21:33:14.3	+25:28:59.1	18.8	15.2
4FGL J2350.6-3005	3HSP J235034.3-300604	IC-190104A	3.32	23:50:34.3	-30:06:03.2	18.1	15.7
4FGL J2358.1-2853	CRATES J235815-285341	IC-190104A	2.47	23:58:16.9	-28:53:34.0	19.5	14.0

*Notes.* Column 1: *Fermi* name of the target in the 4FGL catalogue (Abdollahi et al. 2022); Column 2: Counterpart name of the  $\gamma$ -ray source; Column 3: IceCube tracks; Column 4: Angular separation (degrees) between the target and the centroid of the IceCube track; Column 5 - 6: Right ascension and declination of the optical counterpart; Column 7: g-magnitude from SDSS survey or PANSTARRS; Column 8: Frequency (in logarithmic scale) of the synchrotron peak.

## 4 RESULTS

The flux calibrated and de-reddened spectra of the neutrino source candidates are displayed in Fig. A1 and are also available in the online database ZBLLAC<sup>3</sup> (Landoni et al. 2020). For each spectrum, we evaluated the signal-to-noise ratio (S/N) in a number of spectral regions (the average value is given in Table 3), and performed a search for emission/absorption lines.

For 12 out of 21 targets we provide a firm redshift (range: 0.0655 – 1.645, median  $\sim 0.3$ ). Except for 4FGL J0545.0+0613c, that displays a quasar spectrum with very broad emission lines (for details see the relevant note in Section 5), all targets show a spectrum consistent with that of a BLL, i.e., characterized by a combination of a non-thermal continuum, described by a power law, and host galaxy features, when relevant. For 10 objects the spectral continuum is well dominated by the non-thermal continuum with spectral index  $\alpha$  ( $F_\lambda \sim \lambda^{-\alpha}$ ) in the 0.2 - 1.4 interval. In the other 10 objects, the spectrum shows the contribution of the elliptical host galaxy and a firm determination of

the redshift (see Table 3) was obtained from typical absorption lines (Ca II 3934,3968 doublet, the G-band 4305, Mg I 5157, Ca+Fe 5269, and Na I 5892). For 4FGL J1321.9+3219 the redshift ( $z = 0.8126$ ) was derived from a single emission line corroborated by a Mg II intervening absorption system (see note in Section 5). For 4 sources (4FGL J1003.4+0205, 4FGL J1055.7-1807, 4FGL J1124.0+2045, and 4FGL J2358.1-2853) a spectroscopic redshift lower limit is provided by the detection of intervening absorption systems due to Mg II and Fe II. For the 5 lineless objects, we can set a redshift lower limit based on the absence of the host galaxy absorptions (assuming a standard average luminosity of  $\langle M(R) \rangle = -22.9$  (Sbarufatti et al. 2005) and on the minimum detectable EW (see details in Paiano et al. 2017a). All redshift measurements are reported in Table 3.

For the targets with host galaxy signatures, we performed a spectral decomposition considering two components, namely: 1. a power law; 2. a template for the host galaxy (Mannucci et al. 2001). The best fit of the decomposition was obtained from the variation of the parameters of the two components (nucleus-to-host ratio [N/H], evaluated at  $\sim 6000$  Å, and spectral slope of the non-thermal component) and imposing the normalization of the fit at about the central wavelength

<sup>3</sup> <https://web.oapd.inaf.it/zbllac/>

**Table 2.** Journal of the observations.

Object Name	E(B-V)	Telescope	Instrument	Date	$t_{\text{exp}}$ (s)	seeing (")	Air Mass
4FGL J0258.1+2030	1.10	GTC	OSIRIS	08 October 2020	9000	1.3	1.1
4FGL J0339.2−1736	0.07	VLT	FORS2	10 October 2020	2700	0.5	1.0
4FGL J0545.0+0613c	0.99	GTC	OSIRIS	10 October 2020	9000	0.8	1.2
4FGL J0658.6+0636	0.22	GTC	OSIRIS	17 November 2020	4599	1.2	1.1
4FGL J0946.2+0104	0.13	VLT	FORS2	07 December 2020	3600	1.1	1.1
4FGL J1003.4+0205	0.02	VLT	FORS2	18/19 December 2020	5400	0.7	1.2
		GTC	OSIRIS	20 December 2020	4500	1.3	1.3
4FGL J1055.7−1807	0.03	VLT	FORS2	23 December 2020	5400	0.4	1.3
4FGL J1124.0+2045	0.02	GTC	OSIRIS	12 December 2020	3600	1.4	1.2
4FGL J1124.9+2143	0.02	GTC	OSIRIS	12 December 2020	3600	1.0	1.1
4FGL J1314.7+2348	0.01	GTC	OSIRIS	11 February 2021	3600	1.5	1.2
4FGL J1321.9+3219	0.02	GTC	OSIRIS	10 February 2021	4500	1.5	1.3
4FGL J1439.5−2525	0.09	VLT	FORS2	08 February 2021	2700	1.1	1.5
4FGL J1507.3−3710	0.06	VLT	FORS2	07 February 2021	2400	0.9	1.2
4FGL J1528.4+2004	0.06	LBT	MODS	08 June 2021	10800	0.7	1.0
4FGL J1702.2+2642	0.05	GTC	OSIRIS	13 June 2020	3600	0.7	1.2
4FGL J1808.2+3500	0.04	LBT	MODS	10 May 2021	10800	1.5	1.0
4FGL J2030.9+1935	0.08	GTC	OSIRIS	30 April 2020	1500	1.0	1.0
				10 October 2020	1500	1.1	1.0
4FGL J2030.5+2235	0.21	LBT	MODS	01 June 2022	7200	0.7	1.0
4FGL J2133.1+2529c	0.10	GTC	OSIRIS	07 October 2020	2700	1.4	1.3
4FGL J2350.6−3005	0.01	VLT	FORS2	12 October 2020	2400	0.8	1.2
4FGL J2358.1−2853	0.02	VLT	FORS2	10 October 2020	5400	0.8	1.1

*Notes.* Column 2: E(B-V) taken from the NASA/IPAC Infrared Science Archive (<https://irsa.ipac.caltech.edu/applications/DUST/>); Column 3: Telescope used for the observation; Column 4: Instrument; Column 5: Date of the observation; Column 6: Total integration time (sec); Column 7: Average seeing during the observation (arcsec); Column 8: Air mass during the observation.

of each spectrum. We found that in all above cases the decomposition is a good representation of the observed spectrum (see Fig. A3). In some cases (e.g. 4FGL J0339.2−1736, 4FGL J1439.5−2525, and 4FGL J2350.6−3005) the optical spectrum is significantly dominated by the host galaxy while in others the non-thermal component is dominant (e.g. 4FGL J1808.2+3500 and 4FGL J2030.9+1935). The accuracy of these decompositions clearly depends on the quality of the spectra and on N/H, the targets with higher N/H having more uncertain host galaxy estimates. We estimated the absolute magnitude of the host galaxy in the R filter, k-corrected using the above galaxy template spectrum<sup>4</sup>.

We used the host galaxy luminosity to derive  $M_{\text{BH}}$  from the  $M_{\text{BH}}-M(R)$  relationship (Labita et al. 2007), as described in Paper II. Since the total magnitude enters in the relationship, we need to correct for the fact that aperture photometry, based on the calibration image, misses some flux. To evaluate this correction we assume that the host galaxies of these targets are similar to other host galaxies of BL Lac objects (giant elliptical with  $\langle R_{\text{eff}} \rangle = 8$  kpc; Falomo, Pian & Treves 2014). Thus from the assumed shape and apparent size of the galaxy and the adopted aperture we derive the magnitude correction. This is in the range of 0.3 − 0.8 mag and depends very little on  $R_{\text{eff}}$ .

In order to test the above correction we performed an image analysis of 6 targets with a substantial contribution from the host galaxies (see Table 6). We used our calibration images (Section 3) to decompose the source into the nucleus (described by the point spread function [PSF]) and a galaxy model convolved with the PSF (see e.g. Liuzzo et al. 2016, and references therein for example of the

adopted method). We then derived the total magnitude of the host galaxy, which was found to be in agreement with those obtained by spectroscopy described above.

Finally we also set the host galaxy luminosity to the present epoch assuming a passive stellar evolution for massive ellipticals (Bressan, Chiosi, & Fagotto 1994). The corrected host galaxy absolute magnitudes, with a typical uncertainty of the order of 0.7, are reported in Table 6 and used to derive  $M_{\text{BH}}$ .

#### 4.1 Host galaxies, emission lines and BH masses

A peculiar characteristic of the BLL class is the weakness (or absence) of spectral lines in the optical spectra. The absorption lines, detectable if the N/H is advantageous and if the spectrum is of good quality in terms of S/N and resolution, are typical of the old stellar population of the host elliptical galaxies. The possible emission lines can arise from region of recent star formation or from the nuclear activity and their properties are crucial to determine their origin and for the source characterization. For 7 objects, of which 6 also with host galaxy signatures in the spectrum, weak ( $\text{EW} < 3 \text{ \AA}$ ) and narrow emission lines of [O II] 3727 and/or [O III] 5007 and/or [N II] 6583 are found. The average [O II] and [O III] line luminosity are  $\sim 1.8 \times 10^{41} \text{ erg s}^{-1}$  and  $\sim 3.5 \times 10^{40} \text{ erg s}^{-1}$ , respectively. See Table 4 for details on the properties of the emission lines.

From the spectral decomposition, for 10 objects with stellar spectral signature we are able to estimate the properties of the host galaxy component over the continuum. On average the host galaxy luminosity of the targets is somewhat fainter ( $\langle M(R) \rangle = -22.5$ ) than the average value of BLLs as derived from HST images ( $\langle M(R) \rangle = -22.9$ ). In particular, in two cases (4FGL J1528.4+2004

<sup>4</sup> This measurement of the absolute magnitude is derived from the flux through the slit and needs to be corrected for the flux slit loss.



**Table 3.** Properties of the optical spectra of the neutrino candidate blazars studied in this work.

Object Name	g	r	S/N	EW <sub>min</sub> (Å)	z	Line type	$\alpha$
4FGL J0258.1+2030	21.0	-	60	0.80	>0.3	h	0.80
4FGL J0339.2-1736	-	14.9	70	-	$0.0655 \pm 0.0005$	e,g	0.9
4FGL J0545.0+0613c	21.1	-	100	-	$1.645 \pm 0.001$	e	-
4FGL J0658.6+0636	19.9	-	60	0.45	>0.5	h	1.30
4FGL J0946.2+0104	-	19.2	80	-	$0.5768 \pm 0.0005$	g	1.0
4FGL J1003.4+0205	19.1	-	130	-	$>0.4695 \pm 0.0005$	i	1.4
4FGL J1055.7-1807	-	20.0	80	-	$>0.8465 \pm 0.0005$	i	0.40
4FGL J1124.0+2045	19.4	-	100	-	$>0.5805 \pm 0.0005$	i	1.40
4FGL J1124.9+2143	19.4	-	120	0.20	>0.60	h	1.25
4FGL J1314.7+2348	17.5	-	300	0.10	>0.50	h	1.10
4FGL J1321.9+3219	18.8	-	180	-	$0.8126 \pm 0.0005$	e,g,i	1.15
4FGL J1439.5-2525	-	17.2	40	-	$0.161 \pm 0.005$	g	0.5
4FGL J1507.3-3710	-	17.7	100	-	$0.239 \pm 0.005$	e,g	0.8
4FGL J1528.4+2004	-	19.7	70	-	$0.64 \pm 0.01$	e,g	1.00
4FGL J1702.2+2642	-	18.1	190	-	$0.3197 \pm 0.0005$	e,g	1.00
4FGL J1808.2+3500	-	16.7	250	-	$0.282 \pm 0.005$	e,g	0.80
4FGL J2030.9+1935	18.0	-	150	-	$0.3662 \pm 0.0005$	e,g	1.40
4FGL J2030.5+2235	-	19.7	40	0.90	>0.50	h	1.35
4FGL J2133.1+2529c	18.8	-	55	-	$0.295 \pm 0.005$	g	0.80
4FGL J2350.6-3005	-	17.4	85	-	$0.233 \pm 0.001$	g	0.70
4FGL J2358.1-2853	-	19.4	110	-	$>1.5425 \pm 0.0005$	i	0.20

*Notes.* Column 2-3: Observed magnitude (g,r) measured from the acquisition image; Column 4: Median S/N of the spectrum; Column 5: Minimum equivalent width (EW<sub>min</sub>) derived in the 5500 - 6500 Å range (provided only in case of featureless spectrum); Column 6: Redshift. The error is evaluated as a combination of the uncertainty of the centroid of the features with the overall accuracy of the wavelength calibration; Column 7: Type of detected line to estimate the redshift: e = emission line, g = galaxy absorption line, i = intervening absorption assuming Mg II 2796,2803 Å identification, h = lower limit based on the lack of detection of host galaxy absorption lines assuming an elliptical host galaxy with  $M(R) = -22.9$ . Since the distribution of BLL host galaxies has a dispersion ( $1\sigma$ ) of  $\sim 0.5$  mag, these limits may change by 0.05-0.1 depending on the redshift limit (see details in [Paiano et al. 2017a](#)). Column-8: Spectral index  $\alpha$  of the continuum described by a power law  $F_\lambda \sim \lambda^{-\alpha}$ ; for the cases with evident signature of the host galaxy (see Fig. A3) the spectral index of the non-thermal component is estimated by the decomposition of the observed spectrum.

and 4FGL J1702.2+2642) the absolute magnitude is about 1 mag fainter than the average for the BLL class.

The central black hole masses are in the interval  $2 \times 10^8 - 8 \times 10^8 M_\odot$  (median  $M_{BH} \sim 5 \times 10^8 M_\odot$ ) (see Table 6). The uncertainty of an individual  $M_{BH}$  depends on both the dispersion of the  $M_{BH}-M(R)$  relationship,  $\sim 0.45$  dex, and the uncertainty (of about a factor of 2) on the estimate of the host galaxy luminosity.

## 5 NOTES ON INDIVIDUAL SOURCES

**4FGL J0258.1+2030:** This source was proposed as a BLL in the BZCAT catalogue ([Massaro et al. 2015](#)) and is quoted as a plausible association with two neutrino events: IceCube-191231A ([GCN#26620](#)) and IceCube-211125A ([GCN#31126](#)). The spectrum is heavily reddened ( $E(B-V)=1.1$ ) and appears featureless (see Fig. A1). The continuum is described by a power-law shape ( $\alpha \sim 0.8$ ), which confirms the BLL classification of the target. No emission lines with  $EW > 0.8$  Å are found and from the absence of the absorption lines of the host galaxy, we can set a redshift lower limit  $z > 0.3$ , consistent with the previous result of [Shaw et al. \(2013\)](#).

**4FGL J0339.2-1736:** In our spectrum we clearly detect absorption lines ( $H_\beta$ , Mg I, Ca+Fe, and  $H_\alpha$ ) from the host galaxy at  $z = 0.0656$  confirming the redshift proposed by [Jones et al. \(2009\)](#) from the 6dF Survey spectrum based on Ca II absorption. In addition we also detect a faint emission line at 7015 Å ( $EW \sim 1.15$  Å) attributed to [N II] 6584 at the same redshift. The decomposition

of the spectrum into an elliptical galaxy and nucleus described by a power-law ( $\alpha=0.9$ ) yields an N/H = 0.5 (see Fig. A3).

**4FGL J0545.0+0613c:** The optical spectrum exhibits two prominent and broad emission lines at  $\sim 5030$  Å ( $EW \sim 70$  Å) and  $\sim 7400$  Å ( $EW \sim 17.5$  Å) and a weaker emission line at  $\sim 5485$  Å. We identify these lines as C III] 1909 (FWHM = 125 Å) and Mg II 2796,2803 (FWHM = 60 Å) at  $z = 1.645$ . In addition, a broad absorption feature ( $EW \sim 20$  Å) is present on the blue side of C III] emission line. The spectral characteristics are typical of low ionization broad absorption lines (LoBAL) quasars ([Chen et al. 2022](#)).

**4FGL J0658.6+0636:** This source is classified as blazar candidate of uncertain type (BCU) in the 4FGL-DR3 catalogue and with a possible detection up to very high energy ( $E > 100$  GeV) (Atel#14200, [Buson, Garrappa, & Cheung 2020](#)). It was proposed as a plausible association to the neutrino event IceCube 201114A ([GCN#28887](#)). This object is significantly reddened ( $E(B-V) = 0.22$ ). The optical spectrum is featureless and well described by a power law ( $\alpha \sim 1.3$ ) typical of a BLL. We set an EW limit  $< 0.45$  Å for any emission/absorption lines. From the absorption line limit we can set a redshift lower limit  $z > 0.5$  assuming a standard elliptical host galaxy. No previous optical spectra are found in literature.

**4FGL J0946.2+0104:** A noisy spectrum of the source is obtained by the SDSS survey where the Ca II doublet is detected at  $z = 0.577$ . In our better quality spectrum (S/N $\sim 80$ ), in addition

**Table 4.** Properties of the emission lines of BLL objects.

Object Name	z	$\lambda$ (Å)	EW (Å)	Line ID	L (line) ( $\times 10^{40}$ erg s $^{-1}$ )
4FGL J0339.2–1736	0.0655	7015	$1.10 \pm 0.05$	[NII] 6583	4.2
		5335	<0.8	[OIII] 5007	$\leq 2.7$
4FGL J0946.2+0104	0.5768	5876	<0.4	[OII] 3727	$\leq 4.0$
4FGL J1321.9+3219	0.8126	6755	$1.5 \pm 0.1$	[OII] 3727	56
4FGL J1439.5–2525	0.161	5813	<1.3	[OIII] 5007	$\leq 3.5$
4FGL J1507.3–3710	0.239	6203	$3.2^* \pm 0.2$	[OII] 3727	14
		6203	$1.05 \pm 0.15$	[OIII] 5007	4.7
		8340	$1.25 \pm 0.25$	[SII] 6731	5.0
4FGL J1528.4+2004	0.64	6110	$2.80 \pm 0.1$	[OII] 3727	23
4FGL J1702.2+2642	0.3197	4918	$0.55 \pm 0.05$	[OII] 3727	4.1
		6608	$0.4 \pm 0.1$	[OIII] 5007	2.4
4FGL J1808.2+3500	0.282	4778	$0.30 \pm 0.05$	[OII] 3727	5.6
		6419	$0.30 \pm 0.05$	[OIII] 5007	4.8
		8440	$0.15 \pm 0.05$	[NII] 6583	2.0
4FGL J2030.9+1935	0.3662	5092	$0.50 \pm 0.05$	[OII] 3727	8.7
		6840	$0.20 \pm 0.05$	[OIII] 5007	2.6
4FGL J2133.1+2529c	0.295	4826	<3	[OII] 3727	$\leq 15$
		6484	<1.5	[OIII] 5007	$\leq 9.0$
4FGL J2350.6–3005	0.233	6173	<0.3	[OIII] 5007	$\leq 1.4$

Notes. Column 2: Redshift; Column 3: Barycenter of the detected line; Column 4: Measured EW of the line; Column 5: Line identification; Column 6: Line luminosity.

(\*) The [O II] emission line is detected at the very blue edge of the spectral range and a fraction of the signal is lost.

**Table 5.** Equivalent width of the main host galaxy absorption lines.

Object Name	Redshift	Ca II (H,K) (Å)	G-band (Å)	Mg I 5175 (Å)	Na I 5892 (Å)
4FGL J0339.2–1736	0.0655	-	-	$2.6 \pm 0.2$	-
4FGL J0946.2+0104	0.5768	$7.5 \pm 0.3$	$3.8 \pm 0.3$	-	-
4FGL J1439.5–2525	0.161	-	$4.9 \pm 0.5$	$4.0 \pm 0.3$	$2.8 \pm 0.2$
4FGL J1507.3–3710	0.239	$4.7 \pm 0.2$	$2.4 \pm 0.2$	$2.0 \pm 0.2$	-
4FGL J1528.4+2004	0.64	$2.0 \pm 0.4$	-	-	-
4FGL J1702.2+2642	0.3197	$0.30 \pm 0.05$	-	-	-
4FGL J1808.2+3500	0.282	$0.34 \pm 0.1$	-	-	-
4FGL J2030.9+1935	0.3662	$0.90 \pm 0.05$	-	-	-
4FGL J2133.1+2529c	0.295	$6.5 \pm 0.4$	$1.3 \pm 0.4$	$2.5 \pm 0.4$	-
4FGL J2350.6–3005	0.233	$6.2 \pm 0.4$	$2.2 \pm 0.4$	$2.8 \pm 0.2$	$3.6 \pm 0.2$

Column 1: Name of the target; Column 2: Redshift; Column 3: EW of the doublet CaII 3934, 3968 Å; Column 4: EW of G-band 4304 Å; Column 5: EW of Mg I 5175 Å blend; Column 6: EW of Na I 5892 Å. EW measurements and errors follow the procedure outlined in Section 4 for the emission lines.

to Ca II, we clearly detect the G-band absorption line yielding a redshift of  $z = 0.5768$  (see Fig. A1). The spectrum is dominated by a non-thermal component ( $N/H = 11$ ; see Fig. A3).

**4FGL J1003.4+0205:** The optical spectrum secured by SDSS is featureless, although the automatic procedure proposed  $z = 1.4$ . Our high quality ( $S/N \sim 190$ ) spectrum obtained at the VLT appears featureless and well described by a power law with  $\alpha \sim 1.4$ . No emission/absorption features are apparent at level of  $EW = 0.20$  Å and we can set a redshift lower limit  $> 0.75$  from the non-detection of the absorption lines of the host galaxy. We also obtained another spectrum at GTC that covers better the blue part of the spectral range down to 3900 Å. At  $\sim 4115$  Å we can detect an intervening absorption system due to Mg II 2796,2803 (see Fig. A2) allowing us to set a spectroscopic redshift lower limit  $\geq 0.469$ . In the following we conservatively adopt this value, as it requires no assumption on

the presence of emission/absorption features.

**4FGL J1055.7–1807:** In the optical spectrum ( $S/N \sim 80$ ) there are two absorption doublets at 4774, 4801 Å and 5163, 5176 Å, which are attributed to intervening Fe II 2586,2600 and Mg II 2796,2803 systems, respectively, yielding a robust spectroscopic lower limit  $\geq 0.8465$ . The spectral shape is well described by a power law ( $\alpha = 0.4$ ) confirming the BLL classification. No other spectra are found in the literature.

**4FGL J1124.0+2045:** In our spectrum ( $S/N \sim 100$ ), well described by a power law with  $\alpha \sim 1.40$ , we detect a faint absorption doublet system ( $EW \sim 0.6$  Å) at 4419,4430 Å that is attributed to intervening Mg II 2796,2803 cold gas, yielding a spectroscopic redshift lower limit  $\geq 0.5805$ . The same line system appears in the SDSS spectrum, but it was not previously identified.

**Table 6.** Absolute magnitudes of the host galaxies and black hole mass estimates.

Object Name	$z$	N/H	$M(R)$	$\log(M_{\text{BH}}/M_{\odot})$
4FGL J0339.2–1736*	0.0655	0.5	–22.6	8.7
4FGL J0946.2+0104*	0.5768	11	–23.0	8.9
4FGL J1439.5–2525*	0.161	0.25	–22.8	8.8
4FGL J1507.3–3710*	0.239	3	–22.3	8.6
4FGL J1528.4+2004*	0.64	11	–22.1	8.4
4FGL J1702.2+2642	0.3197	11	–21.9	8.3
4FGL J1808.2+3500	0.282	8	–22.6	8.7
4FGL J2030.9+1935	0.3662	14	–22.6	8.7
4FGL J2133.1+2529c	0.295	2.2	–22.8	8.8
4FGL J2350.6–3005*	0.233	1.0	–22.7	8.7

*Notes.* Column 2: Redshift; Column 3: N/H estimated through the slit, i.e. the ratio of the fluxes of the nucleus to the host galaxy at 6000 Å; Column 4: Absolute magnitude of the host galaxy in the R filter; Column 5: Logarithm of  $M_{\text{BH}}$  in solar units derived through the  $M_{\text{BH}}-M(R)$  relationship. The absolute magnitude of the host galaxy is estimated by the decomposition of the optical spectra as the sum of a power law and an elliptical galaxy template. The associated error is dominated by the dispersion ( $\sim 0.45$  dex) of the  $M_{\text{BH}}-M(R)$  relation (Labita et al. 2007). For the sources marked with the asterisk (\*), we performed the decomposition of the acquisition image in order to compare the host galaxy magnitude obtained with the imaging and with the spectral decomposition plus the slit loss correction (see text in Sec 4.)

**4FGL J1124.9+2143:** Neither absorption nor emission features are present in our good spectrum (S/N $\sim 120$ ) that is well described by a power law ( $\alpha \sim 1.25$ ) typical of BLL. From the minimum EW = 0.20 Å of absorption lines of the host galaxy, we set a redshift lower limit  $> 0.6$ . There is an SDSS spectrum of the source that appears featureless.

**4FGL J1314.7+2348:** Optical spectra reported in Massaro et al. (2014); Paggi et al. (2014); Shaw et al. (2013) and in the SDSS database are featureless, although Massaro et al. (2014) quoted an SDSS uncertain redshift of 0.15, which we used in Paper II. Also our very high quality (S/N $\sim 300$ ) spectrum does not exhibit emission/absorption lines and shows the typical BLL power law shape ( $\alpha \sim 1.1$ ). From the estimated minimum EW = 0.10 Å, we set a redshift lower limit  $> 0.50$ .

**4FGL J1321.9+3219:** We obtained a high quality S/N $\sim 180$  spectrum from which we clearly detect an intervening absorption system at 4243,4254 Å that is identified with Mg II 2796,2803 at  $z = 0.5175$ . In addition an emission line at 6755 Å identified as [O II] 3727 yields  $z = 0.8126$ . Note that based on a lower S/N featureless SDSS spectrum and the overall spectral energy distribution (SED) we proposed  $z \sim 0.4$  in Paper II.

**4FGL J1439.5–2525:** No emission lines are found in our spectrum. We detect absorption lines due to the host galaxy, confirming the redshift of 0.161 reported in Desai et al. (2019). From the spectral decomposition in Fig. A3, the contribution of the nucleus is very marginal with N/H $\sim 0.25$ .

**4FGL J1507.3–3710:** We obtain a spectrum with S/N $\sim 100$  which exhibits clear absorption lines attributed to the host galaxy (Ca II 3934,3968, G-band 4305, Mg I 5175, and Na I 5892) and emission lines at 6144,6203 Å attributed to [O III] 4959,5007, yielding  $z = 0.239$ . In addition we detect very faint emission lines due to [N II] and [S II]. The [O II] emission line is detected at the very blue edge of the spectral range and a fraction of the line is lost. No previous spectra are available in literature.

**4FGL J1528.4+2004:** This  $\gamma$ -ray source is unassociated with a lower energy counterpart and unclassified in the 4FGL-DR3

catalogue. However, the source 3HSP J152835.8+200420 (Chang et al. 2019), located well within the 0.005 square degrees error ellipse of the *Fermi*-LAT source, is the likely counterpart since its  $\gamma$ -ray flux and spectral shape are perfectly consistent with the SED of an HSP blazar (see also Paiano et al. 2017). Our LBT and GTC spectra are the first ones obtained for the optical counterpart. Our LBT spectrum is characterized by a power-law continuum with  $\alpha=1$  superimposed on a significant contribution of the host galaxy in the redder part of the spectrum (see Fig. A3), yielding N/H $\sim 11$ . This confirms the BLL classification for the source. We clearly detect an emission line (EW $\sim 2.80$  Å) at 6110 Å attributed to [O II] 3727. The same line is found in a second spectrum taken at the GTC (see the closeup around the line in Fig. A2). The redshift of the source is  $z = 0.64$ . Other three weak absorption features are detected due to the Ca II doublet and the G-band from the stellar component of the host galaxy at the same redshift.

**4FGL J1702.2+2642:** This source was proposed as a plausible association to the neutrino event IceCube 200530A (GCN#27865 and GCN#27879). Our high quality (S/N $\sim 190$ ) optical spectrum exhibits faint emission lines attributed to [O II] 3727 (at 4918 Å, EW = 0.55 Å) and [O III] 5007 (at 6608 Å, EW = 0.40 Å), together with stellar absorption lines of its host galaxy (CaII (3934,3968) at 5191,5237 Å and marginally the G-band 4304 at 5681 Å), yielding  $z = 0.3197$ . From the spectral decomposition (see Fig. A3) of the two components (nucleus and host galaxy), we get N/H = 11. No previous spectra are available in literature.

**4FGL J1808.2+3500:** No spectra are present in the literature for the source. We obtained a S/N $\sim 250$  optical spectrum at the LBT that exhibits emission lines at 4778, 6419, and 8440 Å attributed to [O II] 3727, [O III] 5007, and [N II] 6583 respectively (see Fig. A1 and Table 4). In addition we found weak absorption lines of the Ca II doublet at 5043,5088 Å. The redshift of the source is  $z=0.282$ .

**4FGL J2030.9+1935:** In our good (S/N $\sim 150$ ) optical spectrum, showing the typical BLL non-thermal continuum, we found one emission line at 5092 Å (EW $\sim 0.50$  Å) attributed to [O II] and another very weak (EW $\sim 0.2$  Å) emission feature at 6840 Å consistent with [O III], yielding  $z = 0.3662$ . The G-band is overlapped to the Galactic Na I absorption line. From the spectral decomposition analysis

(see Fig. A3) we get  $N/H = 14$ . In addition, at the same redshift we detect the absorption Ca II doublet due to stellar population of its host galaxy. However, from the analysis of the GTC acquisition image, we are not able to detect the host galaxy ( $M(R) > -22.6$ ). A spectrum of the source was published by Kasai et al. (2023) after we performed our observation and our redshift is compatible with theirs.

**4FGL J2030.5+2235:** This  $\gamma$ -ray source is unassociated in the 4FGL-DR3 catalogue. The likely association with the  $\gamma$ -ray detection is the source 3HSP J203031.6+223439, well located inside the *Fermi*-LAT error ellipse and with a broad-band SED typical of an HSP blazar. The optical spectrum ( $S/N \sim 40$ ), obtained at LBT, is featureless and well described by a power law continuum ( $\alpha \sim 1.35$ ). Based on the absence of host galaxy lines we can set a redshift lower limit  $> 0.5$ .

**4FGL J2133.1+2529c:** Our optical spectrum clearly shows absorption lines due to the elliptical galaxy stellar population, in particular the Ca II 3934,3968 doublet, G-band 4305, and Mg I 5157 at  $z = 0.295$ . This value is in agreement with that reported by Massaro et al. (2015) and adopted by Chang et al. (2019). From our decomposition analysis (see Fig. A3), we get  $N/H \sim 2$  and  $\alpha = 0.8$  for the nuclear power-law component.

**4FGL J2350.6–3005:** The optical spectrum displays the typical absorption lines (Ca II, G-band,  $H_\beta$  and Mg I, Ca+Fe, Na I) due to the old stellar population of the host galaxy at  $z = 0.233$ . The decomposition analysis (Fig. A3) shows the presence of the host galaxy component with a moderate non-thermal nucleus emission ( $N/H \sim 1$ ) described by a power law with index  $\alpha = 0.7$ .

**4FGL J2358.1–2853:** The spectrum exhibits a non-thermal continuum described by a power law ( $\alpha \sim 0.20$ ). We detect a strong absorption doublet ( $EW \sim 10 \text{ \AA}$ ) at 7106, 7124  $\text{\AA}$  that corresponds to a Mg II 2796,2803 intervening absorption systems at  $z = 1.5415$  (see Fig. A1), with other two absorption features found at 6054 and 6608  $\text{\AA}$  due to Fe II at the same redshift. Moreover, we find three additional absorption systems at 5270  $\text{\AA}$ ,  $\sim 5730 \text{ \AA}$ , and  $\sim 6200 \text{ \AA}$  corresponding to Fe II and Mg II intervening at  $z = 1.2123$ .

## 6 SOURCE CHARACTERIZATION

We now characterize the new sources belonging to the G20 sample using the data discussed above and in Paper II, Section 3 (where details on the radio and  $\gamma$ -ray data and  $\nu_{\text{peak}}^S$  derivation can be found). The extra sources are discussed in Section 7. One of the issues we want to address is that of the so-called “masquerading” BLLs. Padovani et al. (2019) showed that TXS 0506+056, the first plausible non-stellar neutrino source is, despite appearances, *not* a blazar of the BL Lac type but instead a masquerading BLL. This class was introduced by Giommi et al. (2012); Giommi, Padovani, & Polenta (2013) (see also Ghisellini et al. 2011) and includes sources which are in reality Flat Spectrum Radio Quasars (FSRQs) whose emission lines are washed out by a very bright, Doppler-boosted jet continuum, unlike “real” BLLs, which are *intrinsically* weak-lined objects. This is extremely important for two reasons: (1) “real” BLLs and FSRQs turn out to belong to two very different physical classes, i.e., objects without and with high-excitation emission lines in their optical spectra, referred to as low-excitation (LEGs) and high-excitation galaxies (HEGs), respectively (e.g. Padovani et al. 2017, and references therein); (2) masquerading BLLs, being HEGs, benefit from

several radiation fields external to the jet (i.e., the accretion disc, photons reprocessed in the broad-line region (BLR) or from the dusty torus), which, by providing more targets for the protons, might enhance neutrino production as compared to LEGs.

Padovani et al. (2019) and Paper II, to which we refer the reader for more details, used the following four parameters for this classification, in decreasing order of relevance: (1) location on the radio power – [O II] emission line power,  $P_{1.4\text{GHz}} - L_{[\text{O II}]}$ , diagram, which defines the locus of jetted (radio-loud) quasars; (2) a radio power  $P_{1.4\text{GHz}} > 10^{26} \text{ W Hz}^{-1}$ , since HEGs become the dominant population in the radio sky above this value; (3) an Eddington ratio, i.e., the ratio between the (accretion-related) observed luminosity,  $L_{\text{acc}}$ , and the Eddington luminosity<sup>5</sup>,  $L_{\text{acc}}/L_{\text{Edd}} \gtrsim 0.01$ , which is typical of HEGs (Padovani et al. 2017); (4) a  $\gamma$ -ray Eddington ratio  $L_\gamma/L_{\text{Edd}} \gtrsim 0.1$ , where  $L_\gamma$  is the rest-frame, k-corrected,  $\gamma$ -ray power between 0.1 and 100 GeV, derived by integrating the *Fermi* best-fit spectra, together with  $1\sigma$  statistical uncertainties, as described in Sect. 3.3 of Paper II. The derivation of the thermal, accretion-related bolometric luminosity is not easy for BLLs and it involves  $L_{[\text{O II}]}$  and  $L_{[\text{O III}]}$  (see Punsly & Zhang 2011, Padovani et al. 2019 and Paper II). For two sources (down from five in Paper II) for which we have no line information we got an upper limit on  $L_{\text{disc}}$  from Paliya et al. (2021), which implies  $L_{\text{acc}} < 2 \times L_{\text{disc}}$ .

We anticipate that no object is classified as masquerading based only on  $L_{\text{acc}}/L_{\text{Edd}}$  and/or  $L_\gamma/L_{\text{Edd}}$ , which are the least certain parameters given their dependence on the accretion power,  $L_{\text{acc}}$ , and  $M_{\text{BH}}$  (see Section 4.1). Moreover, the LEGs – HEGs dividing lines for these two parameters are somewhat blurry and not clear-cut. In practice, then, the Eddington ratios are used mostly as a consistency check.

Table 7 gives the main properties of the new objects and of the sources for which we have better or new estimates for some parameters (the latter marked by an asterisk). Namely, name (column 1), *Fermi*-4FGL name (column 2), redshift (column 3), rest-frame  $\nu_{\text{peak}}^S$  (column 4),  $P_{1.4\text{GHz}}$  (column 5),  $L_{[\text{O II}]}$  and  $L_{[\text{O III}]}$  (columns 6 and 7),  $M_{\text{BH}}$  (column 8),  $L_{\text{acc}}/L_{\text{Edd}}$ ,  $L_\gamma$ , and  $L_\gamma/L_{\text{Edd}}$  (columns 9, 10, and 11). When  $M_{\text{BH}}$  is missing we assumed a value of  $6.3 \times 10^8 M_\odot$  (e.g., Paper II and references therein). Note that, as mentioned in Paper II, 5BZB J1322+3216 (a.k.a. 4C+32.43) has a very steep ( $\nu^{-0.8}$  between 130 MHz and 4.8 GHz) radio spectrum. Its large radio power is therefore also due to extended emission and not only to a strong core, unlike the other sources, which are characterized by a flat radio spectrum, and we made a correction for this<sup>6</sup>.

Table 8 lists all masquerading BLLs in the G20’s sample, including for completeness also those discussed in Paper II, with the conditions they fulfil. All sources satisfy at least two criteria.

### 6.1 Statistical Analysis

We now present updated versions of Figs. 1 – 3 of Paper II, which were used to discuss the multi-wavelength properties of the G20’s

<sup>5</sup> The Eddington luminosity is  $L_{\text{Edd}} = 1.26 \times 10^{46} (M/10^8 M_\odot) \text{ erg s}^{-1}$ , where  $M_\odot$  is one solar mass.

<sup>6</sup> This was done by using the peak flux at 1.4 GHz from the FIRST survey (White et al. 1997), which is  $\sim 40$  per cent smaller than the NVSS value (Condon et al. 1998). We remark that this source appears to be anomalous as a blazar based on its steep radio spectrum and compact radio image (Gordon et al. 2020). Still, it is strongly variable, namely by a factor of 2 in the  $3.4 \mu\text{m}$  band in about six months, based on NEOWISE data (Mainzer et al. 2014).



**Table 7.** New and updated source properties.

Name	4FGL name	$z$	$\nu_{\text{peak}}^S$ [Hz]	$P_{1.4\text{GHz}}$ [W Hz <sup>-1</sup> ]	$L_{[\text{O II}]}$ [erg s <sup>-1</sup> ]	$L_{[\text{O III}]}$ [erg s <sup>-1</sup> ]	$M_{\text{BH}}$ [ $M_{\odot}$ ]	$L_{\text{acc}}/L_{\text{Edd}}$	$L_{\gamma}$ [erg s <sup>-1</sup> ]	$L_{\gamma}/L_{\text{Edd}}$
3HSP J033913.7–173600*	4FGL J0339.2–1736	0.0655	15.6	24.22	...	<40.4	8.7	<-2.2	43.9	-2.9
3HSP J094620.2+010451*	4FGL J0946.2+0104	0.5768	>18.2	25.11	<40.6	<40.5	8.9	<-2.0	45.7	-1.3
3HSP J100326.6+020455	4FGL J1003.4+0205	>0.469	16.0	>24.53	...	...	...	...	>45.1	>-1.8
VOU J105603–180929	4FGL J1055.7–1807	>0.8465	14.4	>25.36	...	...	...	...	>45.3	>-1.6
3HSP J112405.3+204553	4FGL J1124.0+2045	>0.5805	15.5	>24.89	...	...	...	...	>45.4	>-1.5
3HSP J112503.6+214300	4FGL J1124.9+2143	>0.6	16.0	>24.88	...	...	...	...	>45.2	>-1.7
5BZB J1314+2348*	4FGL J1314.7+2348	>0.5	>14.2	>26.07	...	...	...	...	>46.0	>-0.9
5BZB J1322+3216*	4FGL J1321.9+3219	0.8126	14.8	26.83	41.8	...	...	-1.3	45.7	-1.2
VOU J143934–252458*	4FGL J1439.5–2525	0.161	14.1	24.33	...	<40.5	8.8	<-2.2	44.1	-2.8
VOU J150720–370902	4FGL J1507.3–3710	0.239	14.6	25.04	41.2	40.7	8.6	-1.6	44.7	-2.0
3HSP J152835.7+20042*	4FGL J1528.4+2004	0.64	16.4	24.57	41.4	...	8.4	-1.0	45.3	-1.2
CRATES J180812+350104	4FGL J1808.2+3500	0.282	14.6	25.26	40.8	40.7	8.7	-1.8	45.1	-1.7
3HSP J203031.6+223439	4FGL J2030.5+2235	>0.5	16.4	>24.53	...	...	...	...	>45.1	>-1.8
3HSP J203057.1+193612	4FGL J2030.9+1935	0.3662	15.9	25.28	40.9	40.4	8.7	-1.8	45.4	-1.4
3HSP J213314.3+252859*	4FGL J2133.1+2529	0.295	15.3	24.93	<41.3	<40.9	8.8	<-1.8	44.9	-2.0
3HSP J235034.3–300604*	4FGL J2350.6–3005	0.233	15.8	24.70	...	<40.4	8.7	<-2.2	44.8	-2.0
CRATES J235815–285341	4FGL J2358.1–2853	>1.5425	14.4	>27.01	...	...	...	...	>46.7	>-0.2

*Notes.* Column 1: name; column 2 *Fermi*-4FGL name; column 3: redshift; column 4: rest-frame  $\nu_{\text{peak}}^S$ ; column 5:  $P_{1.4\text{GHz}}$ ; column 6:  $L_{[\text{O II}]}$ ; column 7:  $L_{[\text{O III}]}$ ; column 8:  $M_{\text{BH}}$ ; column 9:  $L_{\text{acc}}/L_{\text{Edd}}$ ; column 10:  $L_{\gamma}$ ; column 11:  $L_{\gamma}/L_{\text{Edd}}$ . All values, apart from redshift, are in logarithmic scale. An asterisk denotes sources, which have updated/improved data (redshifts, line powers, masses) as compared to Tab. 1 of Paper II.

**Table 8.** Whole sample masquerading BLL properties.

Name	IceCube Name	$z$	$P_{1.4\text{GHz}} - L_{[\text{O II}]}$	$P_{1.4\text{GHz}}$	$L_{\text{acc}}/L_{\text{Edd}}$	$L_{\gamma}/L_{\text{Edd}}$
3HSP J010326.0+15262	IC160331A	0.2461	✓	I	✓	✗
5BZU J0158+0101	IC090813A	0.4537	✓	I	✓	✓
TXS 0506+056	IC170922A	0.3365	✓	✓	✓	✓
CRATES J052526–201054	IC150428A	0.0913	✓	I	✓	✗
GB6 J1040+0617	IC141209A	0.74	✓	I	✓	✓
3HSP J111706.2+20140	IC130408A	0.138	✓	I	✓	✗
5BZB J1314+2348	IC151017A	>0.5	–	✓	–	✓
5BZB J1322+3216	IC120515A	0.8126	✓	✓	✓	✗
3HSP J143959.4–23414	IC170506A	0.309	✓	I	✓	✗
VOU J150720–370902	IC181014A	0.239	✓	I	✓	✗
3HSP J152835.7+20042	IC110521A	0.64	✓	I	✓	✗
CRATES J180812+350104	IC110610A	0.282	✓	I	✓	✗
3HSP J203057.1+193612	IC100710A	0.3662	✓	I	✓	✗
5BZB J2227+0037	IC140114A	>1.0935	–	✓	–	✓
CRATES J232625+011147	IC160510A	1.595	–	✓	✗	✓
CRATES J235815–285341	IC190104A	>1.5425	–	✓	–	✓

*Notes.* ‘✓’ implies that the condition is met, ‘I’ that the condition is not met but this does not mean this is not a masquerading BLL, ‘✗’ that the condition is not met, and ‘–’ that no information is available.

sample. We anticipate that the figures confirm with larger statistics the trends highlighted in Paper II. We used the following software: *fit* (Press et al. 1992) to fit data to a straight line (linear regression), with the correlation significance given by the Spearman test (*sppear*: Press et al. 1992; note that exactly the same results were obtained using the Pearson test [*pears*]). The issue of a possible dependence of the correlations between powers on the common redshift dependence was dealt with by using a partial correlation analysis (e.g. Padovani 1992); ASURV (Lavalley, Isobe, & Feigelson 1992), the Survival Analysis package, which employs the routines described in Feigelson & Nelson (1985) and Isobe et al. (1986) and, amongst other things, evaluates mean values by trying to deal properly with limits using the Kaplan-Meier estimator. The probability that two samples

are drawn from the same parent population was estimated using a Kolmogorov-Smirnov (KS) test (*kstwo*: Press et al. 1992) and the Peto-Prentice test (Lavalley, Isobe, & Feigelson 1992) in ASURV, which is the least affected by differences in the censoring patterns, which might be present in the two samples. We did not use ASURV for linear regression fits in the presence of lower limits because all its routines require binning and the resulting best fit turned out to depend on the chosen bin size. We have instead tested how the limits affected our results by increasing artificially the lower limits on the powers (see Section 6.3).

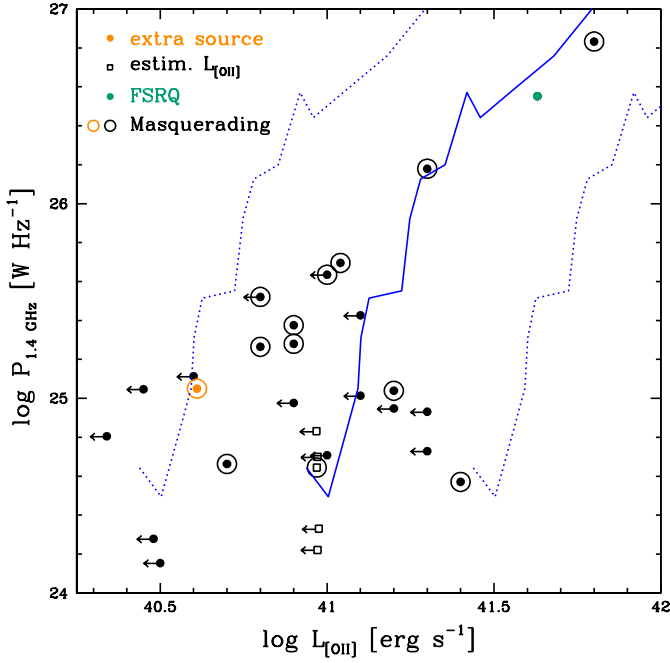


**Figure 1.**  $P_{1.4\text{GHz}}$  vs.  $L_{[\text{O II}]}$  for the objects in our sample with [O II] (or [O III]) information (black filled circles), with masquerading sources highlighted (larger empty circles). Sources for which  $L_{[\text{O III}]}$  has been estimated from  $L_{[\text{O III}]}$  are denoted by black empty squares. The green filled circle indicates the FSRQ in our sample, while the orange point is one of the extra sources (Section 7). The solid blue line is the locus of jetted (radio-loud) quasars, with the two dotted lines indicating a spread of 0.5 dex, which includes most of the points in Fig. 4 of Kalfountzou et al. (2012) (converted from radio powers in  $\text{W Hz}^{-1} \text{sr}^{-1}$  and line powers in W). Arrows denote upper limits on  $L_{[\text{O II}]}$ .

## 6.2 The radio power – emission line diagram ( $P_{1.4\text{GHz}} - L_{[\text{O II}]}$ )

Fig. 1 shows the location of the sources with [O II] information on the  $P_{1.4\text{GHz}} - L_{[\text{O II}]}$  diagram. As done in Paper II we have also added five objects for which only the [O III] flux was available, converting  $L_{[\text{O III}]}$  to  $L_{[\text{O II}]}$  using Fig. 7 of Kalfountzou et al. (2012), marking them differently [open squares] in the figure. Twelve objects<sup>7</sup> are close to the locus of jetted quasars and are therefore “bona fide” masquerading BLLs. All have also  $L_{\text{acc}}/L_{\text{Edd}} \geq 0.01$ . CRATES J024445+132002, the FSRQ in our sample, is also (by definition) very close to the locus. Five more sources have quite stringent  $L_{[\text{O II}]}$  upper limits, two more have  $L_{[\text{O II}]}$  upper limits plus low  $P_{1.4\text{GHz}}$ , while eight more have an upper limit not too far from (or to the right of) the locus. However, given that these latter sources have no other HEG-like property and no [O III] detection, and that we want to keep the selection conservative, we are not including them with the masquerading sources (although some of them are borderline).

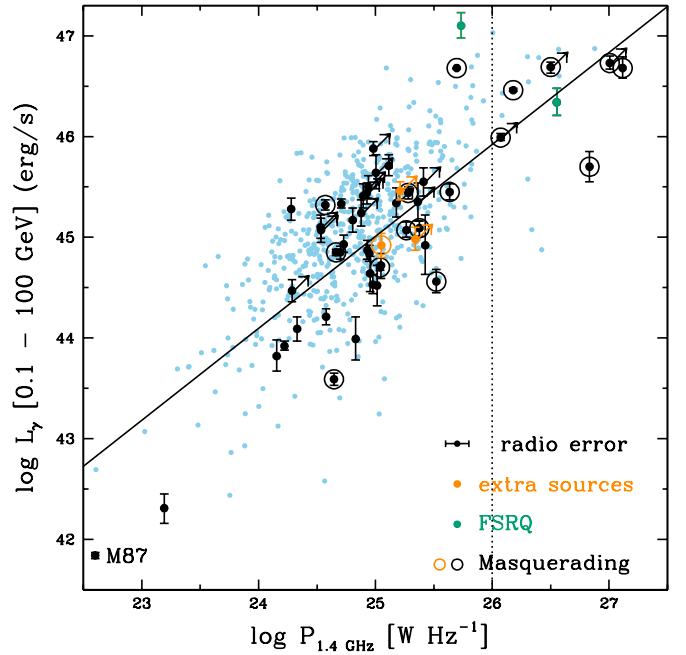


**Figure 2.**  $L_\gamma$  vs.  $P_{1.4\text{GHz}}$  for our sample (black filled circles), with masquerading sources highlighted (larger empty circles). The green filled circle indicates the two FSRQs (the top-left one being also an extra source), while the orange points are the extra sources (Section 7). The radio power for M87, which is labelled, is derived from a time-averaged VLBA core flux at 15 GHz (Kim et al. 2018). Vertical error bars denote the  $1\sigma$  uncertainties on the individual  $\gamma$ -ray powers, while the horizontal error bar represents the typical uncertainty on the radio power due to variability, based on Richards et al. (2011) (see text for details). The solid line is the linear best fit  $L_\gamma \propto P_{1.4\text{GHz}}^{0.90}$ , while the vertical dotted line marks the  $10^{26} \text{ W Hz}^{-1}$  power above which a source is classified as masquerading (see text for details). Arrows denote lower limits on redshift and therefore powers. The small light blue points are the control sample of IBLs and HBLs (Section 8.1).

## 6.3 The $\gamma$ -ray power – radio power diagram ( $L_\gamma - P_{1.4\text{GHz}}$ )

Fig. 2 shows  $L_\gamma$  vs.  $P_{1.4\text{GHz}}$  for our sources (black circles). Vertical error bars denote the  $1\sigma$  uncertainties on the individual  $\gamma$ -ray powers, while the horizontal error bar represents the typical  $1\sigma$  error for the radio band due to variability, derived using the results of Richards et al. (2011) by converting the mean value of their intrinsic modulation index for  $\gamma$ -ray loud blazars to an uncertainty on radio power. We also include the time-averaged very long baseline array (VLBA) core power at 15 GHz for M87, which, given its substantially flat radio spectrum between 15 – 129 GHz, should be representative of its 1.4 GHz core power as well (this source is also part of the G20 sample, as discussed in Paper II). Four more sources get classified as masquerading BLLs thanks to their  $P_{1.4\text{GHz}} > 10^{26} \text{ W Hz}^{-1}$ , all of them with  $L_\gamma/L_{\text{Edd}} > 0.1$ . For these objects we have no [O II] or [O III] information.

Fig. 2 shows a very strong linear correlation between the two pow-

<sup>7</sup> Two of these objects have upper limits on their  $L_{[\text{O II}]}$ , although quite close to the locus, but were still classified as masquerading in Paper II because they also have an [O III] detection and  $L_{\text{acc}}/L_{\text{Edd}} > 0.01$ , with one of them also having  $L_\gamma/L_{\text{Edd}} \sim 0.8$ . Note that the  $L_{[\text{O II}]}$  value for VOU J150720–370902 (4FGL J1507.3–3710) has to be considered a lower limit (Section 5) but even so the source is very close to the quasar locus (see Tab. 7).

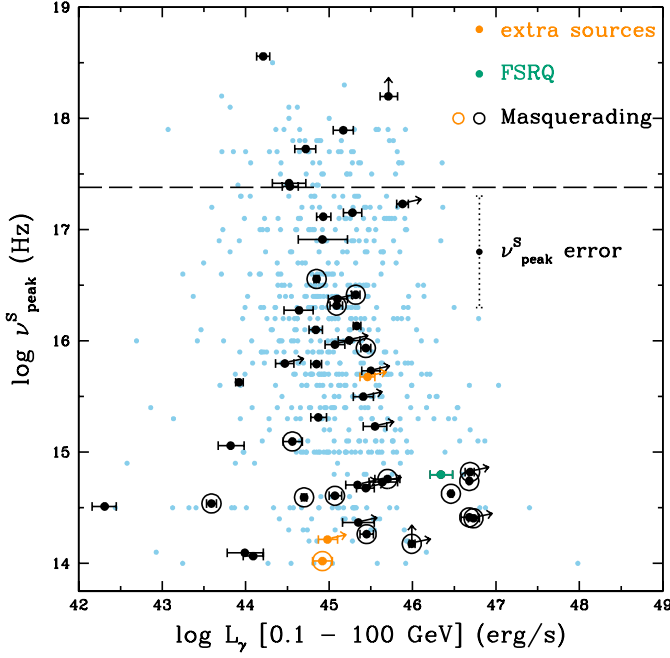


**Figure 3.**  $\nu_{\text{peak}}^S$  vs.  $L_\gamma$  for our sample (black filled circles), with masquerading sources highlighted (larger empty circles). The green filled circle indicates one FSRQ (as the other one has no  $\nu_{\text{peak}}^S$  estimate), while orange points are the extra sources (Section 7). Error bars denote the uncertainties. The typical  $\nu_{\text{peak}}^S$  uncertainty is also shown (vertical dotted line). Arrows denote lower limits on  $\nu_{\text{peak}}^S$  (vertical) and redshifts (diagonal), which also affect the rest-frame  $\nu_{\text{peak}}^S$  values. Sources above the dashed line are extreme blazars (defined as having  $\nu_{\text{peak}}^S > 2 \times 10^{17}$  Hz). The small light blue points are the control sample of IBLs and HBLs (see Section 8.1 for details).

ers, significant at the  $> 99.99$  per cent level<sup>8</sup>, with  $L_\gamma \propto P_{1.4\text{GHz}}^{0.90 \pm 0.11}$ . Removal of the common redshift dependence using a partial correlation analysis (Section 6.1) still gives a 99.2 per cent level significance. The sample includes also fifteen sources with lower limits on their redshifts and therefore on their powers. Since the ASURV routines require binning, with a resulting best fit, which depends on the chosen bin size (Section 6.1), we have tested how this affects our results by increasing artificially the lower limits on the powers by 0.75 dex, which corresponds, for example, to a (large) increase from  $z = 0.7$  to  $z = 1.4$ . The new best fit is  $L_\gamma \propto P_{1.4\text{GHz}}^{1.03 \pm 0.09}$  with the same significance, fully consistent with the previous slope. These slopes are slightly flatter but still consistent with those of Paper II ( $L_\gamma \propto P_{1.4\text{GHz}}^{1.04 \pm 0.13}$  and  $L_\gamma \propto P_{1.4\text{GHz}}^{1.14 \pm 0.11}$  respectively).

The issue of how the properties of masquerading sources might differ from those of the other sources is discussed in Section 8.3.

#### 6.4 The synchrotron peak – $\gamma$ -ray power diagram ( $\nu_{\text{peak}}^S - L_\gamma$ )

Fig. 3 plots the location of our sources (black circles) on the  $\nu_{\text{peak}}^S - L_\gamma$  diagram (note that by definition our sample includes only sources with  $\nu_{\text{peak}}^S > 10^{14}$  Hz). IBLs cover a relatively broad power range, i.e.  $L_\gamma \sim 10^{42} - 10^{47}$  erg s<sup>-1</sup>, while HBLs occupy the narrower

$\sim 10^{44} - 10^{46}$  erg s<sup>-1</sup> region all the way up to  $\nu_{\text{peak}}^S \sim 3 \times 10^{18}$  Hz, although there are also some lower limits on redshift, which means higher  $L_\gamma$  are very likely. Six sources have  $\nu_{\text{peak}}^S > 1$  keV ( $2.4 \times 10^{17}$  Hz) and are therefore classified as extreme, with one very close at  $\nu_{\text{peak}}^S > 1.7 \times 10^{17}$  Hz, given also its redshift lower limit. Note that masquerading BLLs appear to have somewhat lower  $\nu_{\text{peak}}^S$  values; this issue is discussed in Section 8.3.

## 7 THE EXTRA SOURCES

Some targets that were not in the G20 list were also observed. These are still blazars without a redshift determination, which were associated to IceCube tracks after the G20 work was completed and which satisfy in most cases the G20 criteria, as explained in Section 2.

We discuss here these four sources, which are not included in the statistical analysis of Section 6 nor in that of Section 8, with the aim of characterizing them and looking for other masquerading BLLs. Table 9 gives the main properties of the extra sources, where the columns are the same as in Table 7. In the case of NVSS J054341+062553, the FSRQ at  $z = 1.6458$ , we used its Mg II and C III luminosities to estimate the BLR luminosity,  $L_{\text{BLR}}$ , from the composite spectrum of Vanden Berk et al. (2001) (we then derived  $L_{\text{disc}} \sim 10 \times L_{\text{BLR}}$  assuming a standard covering factor of  $\sim 10$  per cent and  $L \sim 20 \times L_{\text{BLR}}$ : see Padovani et al. 2019). Its  $M_{\text{BH}}$  was obtained by applying the virial technique to the Mg II line using the calibration given by Paliya et al. (2021).

One extra source fulfils two criteria for being a masquerading BLL, as shown in Table 10.

## 8 DISCUSSION

### 8.1 Are our sources different from the rest of the blazar population?

To check if our sources are any different from the rest of the blazar population we use a control sample of 783 IBLs and HBLs with  $|b_{\text{II}}| > 30^\circ$ , 630 of which have redshift, detected at the 100 and 97 per cent level in the  $\gamma$ -ray and radio bands, respectively, based on the 3HSP sample (Chang et al. 2019) and an IBL sample put together for this purpose (see Paper II for details).

The location of these objects on the  $L_\gamma - P_{1.4\text{GHz}}$  plane is shown in Fig. 2 (small light blue points), where they appear to populate roughly the same region as our sample. The density of high-power BLLs appears in fact to be larger for our sources, which is likely due to their larger mean redshift (see below). Moreover, the control sample displays a very strong linear correlation between the two powers, significant at the  $> 99.99$  per cent level with  $L_\gamma \propto P_{1.4\text{GHz}}^{0.83 \pm 0.04}$ , consistent with the correlation found for our sample ( $L_\gamma \propto P_{1.4\text{GHz}}^{0.90 \pm 0.11}$ ; Section 6.3). As for the  $\nu_{\text{peak}}^S - L_\gamma$  plane, Fig. 3 shows that the IBL plus HBL control sources, as is the case for Fig. 2, appear to populate the same region as our sample.

We also compared the redshift distribution,  $N(z)$ , of our sources (excluding M87 and the FSRQ), to that of the control sample, as shown in Fig. 4 (black solid and red long-dashed line respectively), taking into account the redshift lower limits using the Kaplan-Meier estimator in ASURV (Section 6.1). The mean redshift is  $\langle z \rangle = 0.66 \pm 0.09$  and  $\langle z \rangle = 0.37 \pm 0.01$  for our sample and the control sample respectively, different at the  $\sim 99.8$  per cent level. The control sample is missing  $\sim 20$  per cent of the redshifts, while we have looked very

<sup>8</sup> We exclude from the fit the FSRQ and M87; this has no influence on the significance or the slope.

**Table 9.** Extra sample properties.

Name	4FGL name	$z$	$\nu_{\text{peak}}^S$ [Hz]	$P_{1.4\text{GHz}}$ [W Hz $^{-1}$ ]	$L_{[\text{O II}]}$ [erg s $^{-1}$ ]	$L_{[\text{O III}]}$ [erg s $^{-1}$ ]	$M_{\text{BH}}$ [ $M_{\odot}$ ]	$L_{\text{acc}}/L_{\text{Edd}}$	$L_{\gamma}$ [erg s $^{-1}$ ]	$L_{\gamma}/L_{\text{Edd}}$
5BZB J0258+2030	4FGL J0258.1+2030	>0.3	14.2	>25.34	...	...	...	...	>45.0	>-1.9
NVSS J054341+062553	4FGL J0545.0+0613	1.645	...	25.73	...	...	9.0	0.0	47.1	0.0
3HSP J065845.0+063711	4FGL J0658.6+0636	>0.5	15.7	>25.21	...	...	...	...	>45.5	>-1.4
5BZB J1702+2643	4FGL J1702.2+2642	0.3197	14.0	25.05	40.6	40.4	8.3	-1.5	44.9	-1.5

Notes. All values, apart from redshift, are in logarithmic scale.

**Table 10.** Masquerading BLL properties: extra sample.

Name	IceCube Name	$z$	$P_{1.4\text{GHz}} - L_{[\text{O II}]}$	$P_{1.4\text{GHz}}$	$L_{\text{acc}}/L_{\text{Edd}}$	$L_{\gamma}/L_{\text{Edd}}$
5BZB J1702+2643	IC200530A	0.3197	✓	I	✓	✗

Notes. ‘✓’ implies that the condition is met, ‘I’ that the condition is not met but this does not mean this is not a masquerading BLL, and ‘✗’ that the condition is not met.

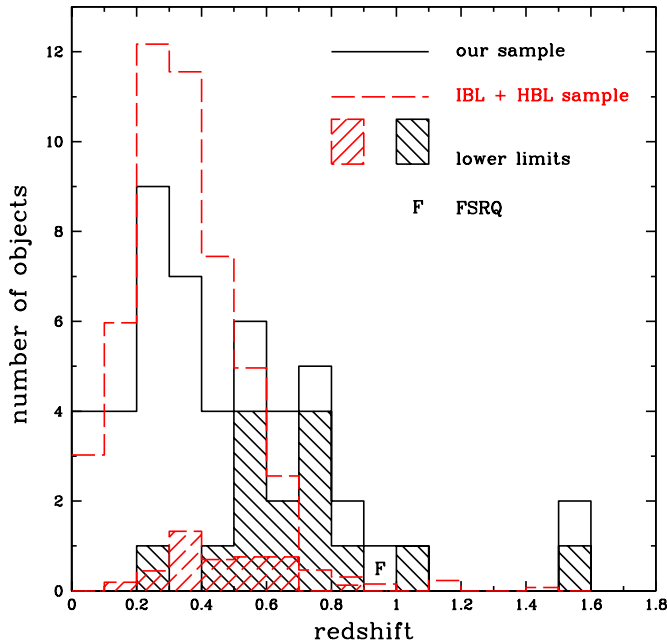


**Figure 4.** The redshift distribution for our sample (black solid line), with lower limits (denoted by the dashed areas). The FSRQ is denoted by an “F”. The red long-dashed line indicates the control sample of IBLs and HBLs scaled to the size of our sample.

carefully for even weak features and obtained a redshift or a lower limit for all the sources we took a spectrum of. Therefore, the fact that the control sample mean redshift is lower than ours is to be expected. This is indeed confirmed by the comparison done in Paper II between our newly determined redshifts and the corresponding values in the Chang et al. (2019)’s sample for sources with a previous redshift estimate, which showed that our redshifts were typically higher by 0.1 and up to  $\gtrsim 0.2$ .

## 8.2 What is the fraction of masquerading BLLs?

We find sixteen masquerading BLLs (Table 8) and eleven sources which fulfil none of our criteria and therefore we consider “bona fide” non-masquerading objects. For twenty sources, however, we do not have the relevant information to make a decision. Therefore, the fraction of masquerading BLLs is in the range 34 – 77 per cent but should be well above the lower bound given our conservative selection (Section 6.2). The corresponding range in Paper II was 24 – 79 per cent, so we have increased by about 40 per cent the value of our lower limit on this fraction.

## 8.3 Do masquerading BLLs have different properties from non-masquerading ones?

All sources in our sample with  $L_{\gamma} \gtrsim 10^{46}$  erg s $^{-1}$  in Fig. 2 are masquerading BLLs, as are all objects with  $P_{1.4\text{GHz}} \gtrsim 10^{25.5}$  W Hz $^{-1}$ . In general, it appears that masquerading BLLs tend to be more powerful than non-masquerading ones (where here we include all 31 sources which are not classified as masquerading). This is confirmed for the radio band, where radio powers are on average  $\sim 9$  times larger and for which a KS test shows that the two samples are significantly different ( $P \sim 99.98$  per cent). A similar result ( $P \sim 98.9$  per cent) is obtained using the Peto-Prentice test (Section 6.1). It could be argued that a high  $P_{1.4\text{GHz}}$  was one of the criteria for selecting masquerading BLLs but not a single source has been classified as such only on the basis of its radio power.  $L_{\gamma}$  is also on average  $\sim 5$  times larger for masquerading BLLs but a KS and a Peto-Prentice test show that the two luminosity distributions are not significantly different. The significant  $P_{1.4\text{GHz}}$  difference is not surprising, as discussed by Padovani et al. (2019) and in Paper II, as masquerading BLLs need to have relatively high powers, besides having  $\nu_{\text{peak}}^S \gtrsim 10^{14}$  Hz, to be able to dilute the quasar-like emission lines, and the radio band is closer to the optical/UV one than the  $\gamma$ -ray band. Masquerading BLLs are also at higher redshift than the rest of the sample but not significantly so ( $P \sim 18$  per cent):  $\langle z \rangle = 0.66 \pm 0.14$  vs.  $\langle z \rangle = 0.54 \pm 0.06$ , where again we have used ASURV (Peto-Prentice and Kaplan-Meier tests). This is likely to be related to their higher powers.

Fig. 3 suggests that  $\nu_{\text{peak}}^S$  might be smaller for masquerading BLLs.



Indeed, using the Kaplan-Meier and Peto-Prentice tests, given the two lower limits on this parameter plus the redshift lower limits, which affects also the rest-frame  $\nu_{\text{peak}}^S$ , we derive  $\langle \log(\nu_{\text{peak}}^S) \rangle = 15.21 \pm 0.22$  vs.  $\langle \log(\nu_{\text{peak}}^S) \rangle = 16.73 \pm 0.26$ , e.g. a 1.5 dex difference, with the two distributions being different at the  $\sim 99.8$  per cent level. As discussed in Paper II, this difference, again, can be explained by a selection effect.

## 9 CONCLUSIONS

We have presented optical spectroscopy of 21 extragalactic sources that are candidates for being the astronomical counterparts of IceCube neutrino events. Apart from one target, which has a quasar-like spectrum, all of the remaining objects have a spectral shape that is fully consistent with a BLL classification. We have provided a firm redshift for twelve sources ( $0.07 < z < 1.6$ ), while for the others we set a lower limit on it. Ten objects have their continuum dominated by non-thermal emission, while in the other ten the spectrum shows the contribution of the elliptical host galaxy.

We have then carefully characterized these sources to determine their real nature, extending to the whole G20 sample the work done in Paper II, to quantify the presence of masquerading BL Lacs, i.e., FSRQs in disguise whose emission lines are swamped by a very strong jet, and to check if these sources were any different from the rest of the blazar population. This was done by assembling a set of ancillary data and by measuring and estimating, in many cases for the first time,  $L_{[\text{O II}]}$  and  $L_{[\text{O III}]}$ , and  $M_{\text{BH}}$ , respectively.

Our main conclusions in this respect are as follows:

(i) we do not find significant systematic differences between the sources studied in this paper and other blazars of the same type, i.e. IBLs and HBLs, in terms of their radio and  $\gamma$ -ray powers, and  $\nu_{\text{peak}}^S$ , while we do for redshift. The lack of such differences might be due to our relatively small sample, given also that less than half of our sources is expected to be associated with IceCube tracks. The redshift difference is instead due to the fact that our control sample is missing  $\sim 20$  per cent of the redshifts, while we have looked very carefully for even weak features and obtained a redshift or a lower limit for all the sources we took a spectrum of;

(ii) the fraction of masquerading BL Lacs in our sample is  $> 34$  per cent and possibly as high as 77 per cent;

(iii) masquerading BL Lacs turn out to be exactly as expected: more powerful than the rest in the radio and  $\gamma$ -ray band, with a smaller  $\nu_{\text{peak}}^S$ . These are the properties, which allow them to effectively dilute their strong, FSRQ-like emission lines.

In subsequent papers we will collect all available multi-wavelength data for the G20 sources and put together their SEDs, and then start modelling them using a lepto-hadronic code to subsequently estimate the expected neutrino emission from each blazar.

## ACKNOWLEDGMENTS

We acknowledge Martina Karl and Theo Glauch for estimating the  $\gamma$ -ray powers for the *Fermi* sources. This work is based on observations collected at the European Southern Observatory under ESO programme 106.213R, at the Gran Telescopio Canarias under the programme GTC2720B, and at the Large Binocular Telescope during the semester 2021A and 2022A. Funding for the Sloan Digital Sky Survey IV has been provided by the Alfred P. Sloan Foundation,

the U.S. Department of Energy Office of Science, and the Participating Institutions. SDSS-IV acknowledges support and resources from the Center for High Performance Computing at the University of Utah. The SDSS website is [www.sdss.org](http://www.sdss.org).

We thank the referee for her/his useful comments and suggestions that allow to improve our manuscript.

## DATA AVAILABILITY

The flux-calibrated and de-reddened spectra are available in our online data base ZBLAC: <https://web.oapd.inaf.it/zblac/>.

## REFERENCES

- Abdo A. A., Ackermann M., Ajello M., et al., 2010, *ApJ*, 716, 30
- Abdollahi S., Acero F., Baldini L., Ballet J., Bastieri D., Bellazzini R., Berenji B., et al., 2022, *ApJS*, 260, 53
- Ahumada R., Prieto C. A., Almeida A., Anders F., Anderson S. F., Andrews B. H., Anguiano B., et al., 2020, *ApJS*, 249, 3
- Appenzeller I., Fricke K., Fürtig W., Gässler W., Häfner R., Harke R., Hess H.-J., et al., 1998, *ESO Messenger*, 94, 1
- Baikal-GVD Collaboration, Erkenov A. K., Kosogorov N. A., Kovalev Y. A., Kovalev Y. Y., Plavin A. V., Popkov A. V., et al., 2022, *arXiv*, arXiv:2210.01650
- Blaufuss E., 2020, <https://gcn.gsfc.nasa.gov/gcn3/28887.gcn3>
- Bressan A., Chiosi C., Fagotto F., 1994, *ApJS*, 94, 63
- Buson S., Garrappa S., Cheung C. C., 2020, *ATel*, 14200
- Buson S., Tramacere A., Pfeiffer L., Oswald L., Menezes R. de ., Azzollini A., Ajello M., 2022, *ApJL*, 933, L43
- Cardelli J. A., Clayton G. C., Mathis J. S., 1989, *ApJ*, 345, 245
- Cepa J., et al., 2003, *SPIE*, 4841, 1739, *SPIE*, 4841
- Chang Y.-L., Arsioli B., Giommi P., Padovani P., Brandt C. H., 2019, *A&A*, 632, A77
- Chen Z., He Z., Ho L. C., Gu Q., Wang T., Zhuang M., Liu G., et al., 2022, *NatAs*, 6, 339
- Condon J. J., Cotton W. D., Greisen E. W., Yin Q. F., Perley R. A., Taylor G. B., Broderick J. J., 1998, *AJ*, 115, 1693
- Desai A., Marchesi S., Rajagopal M., Ajello M., 2019, *ApJS*, 241, 5
- Event Horizon Telescope Collaboration, Akiyama K., Alberdi A., Alef W., Asada K., Azulay R., Baczkó A.-K., et al., 2019, *ApJL*, 875, L1
- Falomo R., Pian E., Treves A., 2014, *A&ARv*, 22, 73
- Feigelson E. D., Nelson P. I. 1985, *ApJ*, 293, 192
- Freudling W., Romaniello M., Bramich D. M., Ballester P., Forchi V., García-Dabó C. E., Moehler S., et al., 2013, *A&A*, 559, A964
- Gargiulo A., Fumana M., Bisogni S., Franzetti P., Cassarà L. P., Garilli B., Scodeggio M., et al., 2022, *MNRAS*, 514, 2902
- Garrappa S., 2020, <https://gcn.gsfc.nasa.gov/gcn3/27879.gcn3>
- Ghisellini G., Tavecchio F., Foschini L., Ghirlanda G., 2011, *MNRAS*, 414, 2674
- Giommi P., Padovani P., Polenta G., Turriziani S., D'Elia V., Piranomonte S., 2012, *MNRAS*, 420, 2899
- Giommi P., Padovani P. & Polenta G., 2013, *MNRAS*, 431, 1914
- Giommi P., Glauch T., Padovani P., Resconi E., Turcati A., Chang Y. L., 2020, *MNRAS*, 497, 865
- Gordon Y. A., Boyce M. M., O'Dea C. P., Rudnick L., Andernach H., Vantghem A. N., Baum S. A., et al., 2020, *RNAAS*, 4, 175
- Hovatta T., Lindfors E., Kiehlmann S., Max-Moerbeck W., Hodges M., Liodakis I., Lähteemäki A., et al., 2021, *A&A*, 650, A83
- IceCube Collaboration, 2013, *Sci*, 342, 6161, 1242856
- IceCube Collaboration, Aartsen M. G., Ackermann M., Adams J., Aguilar J. A., Ahlers M., Ahrens M., et al., 2018a, *Sci*, 361, eaat1378
- IceCube Collaboration et al., 2018b, *Science*, 361, 147
- Isobe T., Feigelson E. D., Nelson P. I., 1986, *ApJ*, 306, 490
- Jones D. H., Read M. A., Saunders W., Colless M., Jarrett T., Parker Q. A., Fairall A. P., et al., 2009, *MNRAS*, 399, 683

Kalfountzou E., Jarvis M. J., Bonfield D. G., Hardcastle M. J., 2012, *MNRAS*, 427, 2401

Kasai E., Goldoni P., Pita S., Williams D. A., Max-Moerbeck W., Hervet O., Cotter G., et al., 2023, *MNRAS*, 518, 2675

Kim J.-Y., Lee S.-S., Hodgson J. A., Algaba J.-C., Zhao G.-Y., Kino M., Byun D.-Y., et al., 2018, *A&A*, 610, L5

Kurahashi N., Murase K., Santander M., 2022, *ARNPS*, 72, 365

Jones D. H., Read M. A., Saunders W., Colless M., Jarrett T., Parker Q. A., Fairall A. P., et al., 2009, *MNRAS*, 399, 683.

Labita M., Treves A., Falomo R., Uslenghi M., 2007, *MNRAS*, 373, 551

Lagunas Gualda C., 2021, <https://gcn.gsfc.nasa.gov/gcn3/31126.gcn3>

Landoni M., Falomo R., Paiano S., Treves A., 2020, *ApJS*, 250, 37

Lavalley M., Isobe T., Feigelson E., 1992, *ASPC*, 25, 245

Liuzzo E., Falomo R., Paiano S., Treves A., Uslenghi M., Arcidiacono C., Baruffolo A., et al., 2016, *AJ*, 152, 38

Mainzer A., Bauer J., Cutri R. M., Grav T., Masiero J., Beck R., Clarkson P., et al., 2014, *ApJ*, 792, 30.

Mannucci F., Basile F., Poggianti B. M., Cimatti A., Daddi E., Pozzetti L., Vanzì L., 2001, *MNRAS*, 326, 745

Massaro F., Masetti N., D'Abrusco R., Paggi A., Funk S., 2014, *AJ*, 148, 66

Massaro F., D'Abrusco R., Landoni M., Paggi A., Masetti N., Giroletti M., Oti-Flóranes H., et al., 2015, *ApJS*, 217, 2

Massaro E., Maselli A., Leto C., Marchegiani P., Perri M., Giommi P., Piranomonte S., 2015, *Ap&SS*, 357, 75

Padovani P., 1992, *A&A*, 256, 399

Padovani P., Giommi P., 1995, *ApJ*, 444, 567

Padovani P., et al., 2017, *A&AR*, 25, 2

Padovani P., Oikonomou F., Petropoulou M., Giommi P., Resconi E., 2019, *MNRAS*, 484, L104

Padovani P., Giommi P., Falomo R., Oikonomou F., Petropoulou M., Glauch T., Resconi E., Treves A., Paiano S., 2022, *MNRAS*, 510, 2671 (Paper II)

Paggi A., Milisavljevic D., Masetti N., Jiménez-Bailón E., Chavushyan V., D'Abrusco R., Massaro F., et al., 2014, *AJ*, 147, 112

Paiano S., Landoni M., Falomo R., Treves A., Scarpa R., Righi C., 2017, *ApJ*, 837, 144

Paiano S., Franceschini A., Stameria A., 2017, *MNRAS*, 468, 4902.

Paiano S., Falomo R., Treves A., Padovani P., Giommi P., Scarpa R., 2021, *MNRAS*, 504, 3338 (Paper I)

Paliya V. S., Domínguez A., Ajello M., Olmo-García A., Hartmann D., 2021, *ApJS*, 253, 46

Plavin A. V., Kovalev Y. Y., Kovalev Y. A., Troitsky S. V., 2021, *ApJ*, 908, 157

Pogge R. W., et al., 2010, *SPIE*, 7735, 77350A, *SPIE*.7735

Press W. H., Teukolsky S. A., Vetterling W. T., Flannery B. P., 1992, *Numerical recipes in FORTRAN. The art of scientific computing*, 2 edn. Cambridge University Press, Cambridge, UK

Punsly B., Zhang S., 2011, *MNRAS*, 412, L123

Resconi E., Coenders S., Padovani P., Giommi P., Caccianiga L., 2017, *MNRAS*, 468, 597

Richards J. L., Max-Moerbeck W., Pavlidou V., King O. G., Pearson T. J., Readhead A. C. S., Reeves R., et al., 2011, *ApJS*, 194, 29

Righi C., Tavecchio F., Inoue S., 2019, *MNRAS*, 483, L127

Santander M., 2019, <https://gcn.gsfc.nasa.gov/gcn3/26620.gcn3>

Sbarufatti B., Treves A., Falomo R., 2005, *ApJ*, 635, 173

Shaw M. S. et al., 2013, *ApJ*, 764, 135

Schlaflly E. F., Finkbeiner D. P., 2011, *ApJ*, 737, 103

Stein R., 2020, <https://gcn.gsfc.nasa.gov/gcn3/27865.gcn3>

Tody D., 1986, *SPIE*, 627, 733, *SPIE*..627

Tody D., 1993, *ASPC*, 52, 173, *ASPC*...52

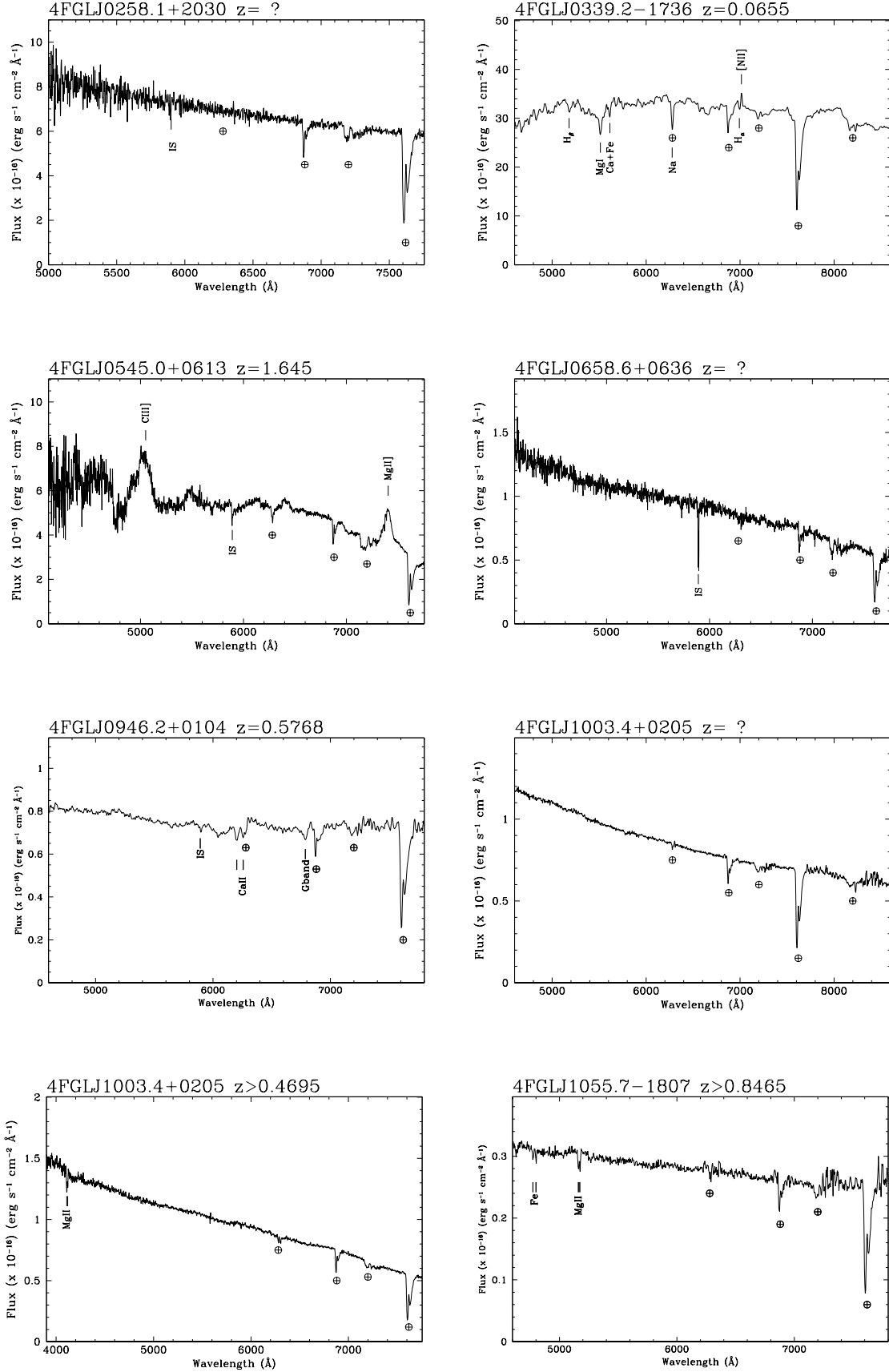
Vanden Berk, D. E., et al., 2001, *AJ*, 122, 549

White R. L., Becker R. H., Helfand D. J., Gregg M. D., 1997, *ApJ*, 475, 479

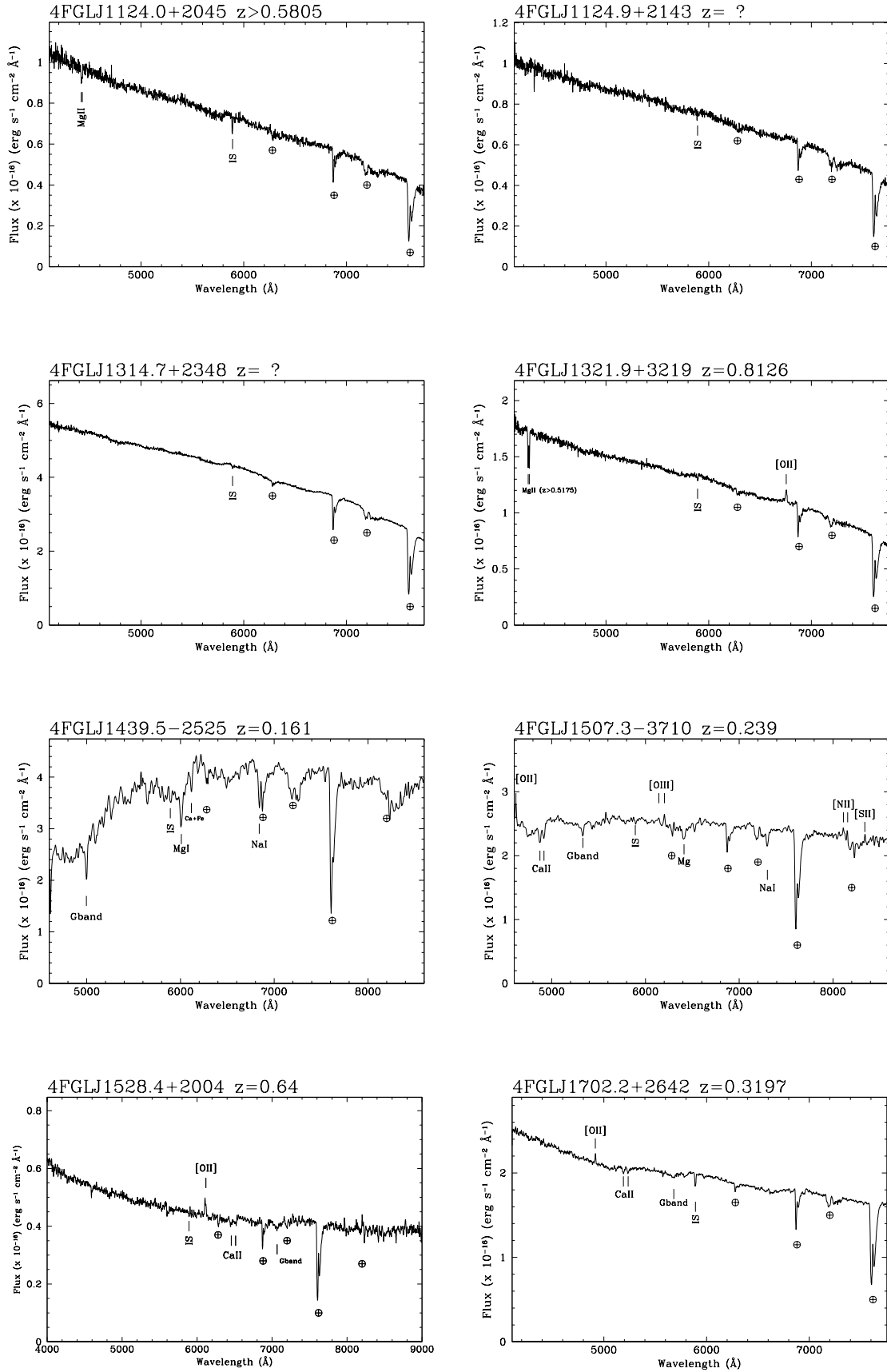
lines (Fig. A2), and spectral decompositions of the observed optical spectra into a power-law and an elliptical template (Fig. A3).

## APPENDIX A:

We show here flux calibrated and de-reddened spectra for our sources (Fig. A1), some examples of close-ups around the detected spectral



**Figure A1.** Flux calibrated and de-reddened spectra of the neutrino candidate blazars obtained at GTC, VLT and LBT (see Table 2 for details). The main telluric bands are indicated by  $\oplus$ , the absorption features from interstellar medium of our galaxies are labelled as IS (Inter-Stellar).

Figure A1. - *Continued*



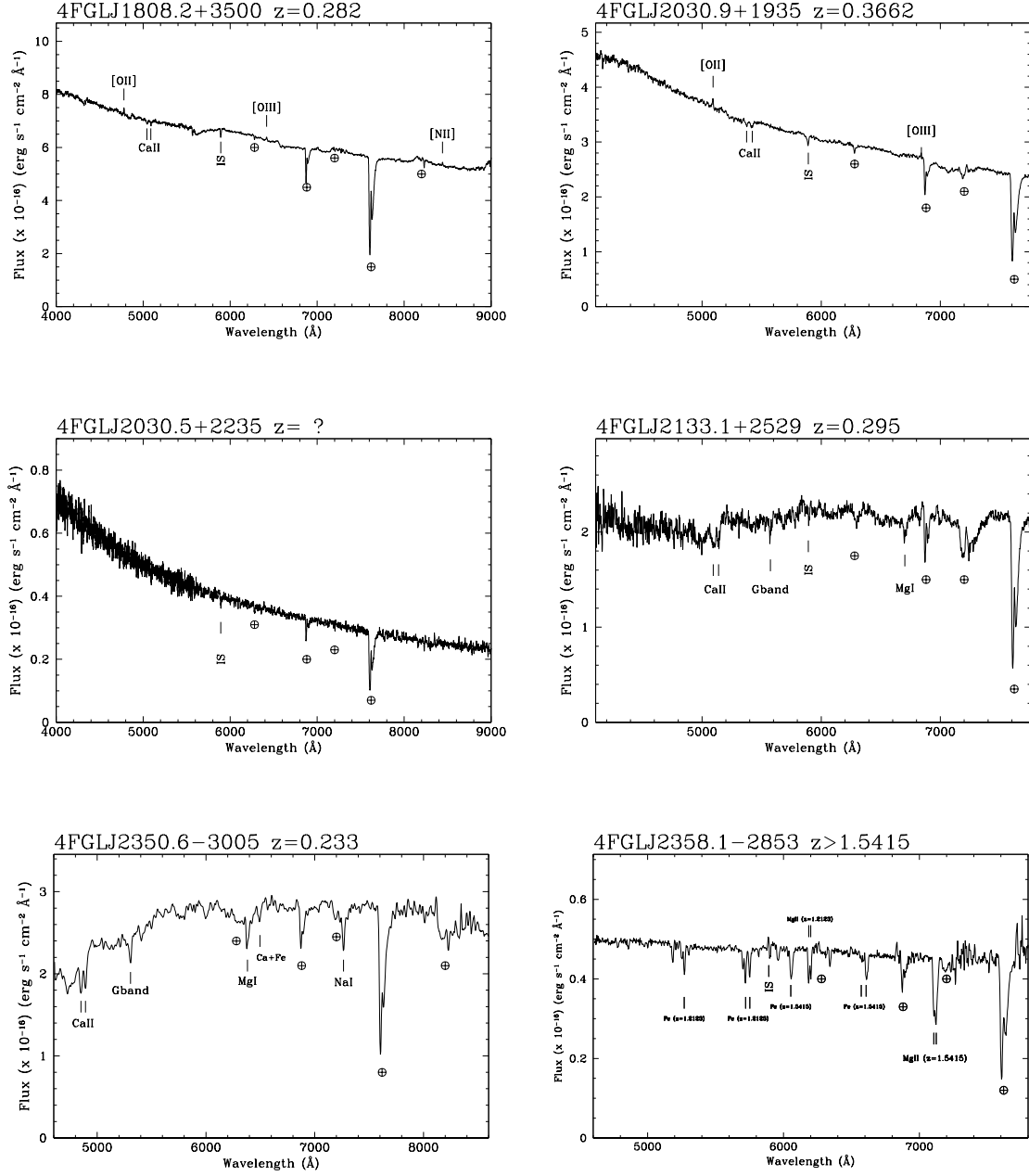
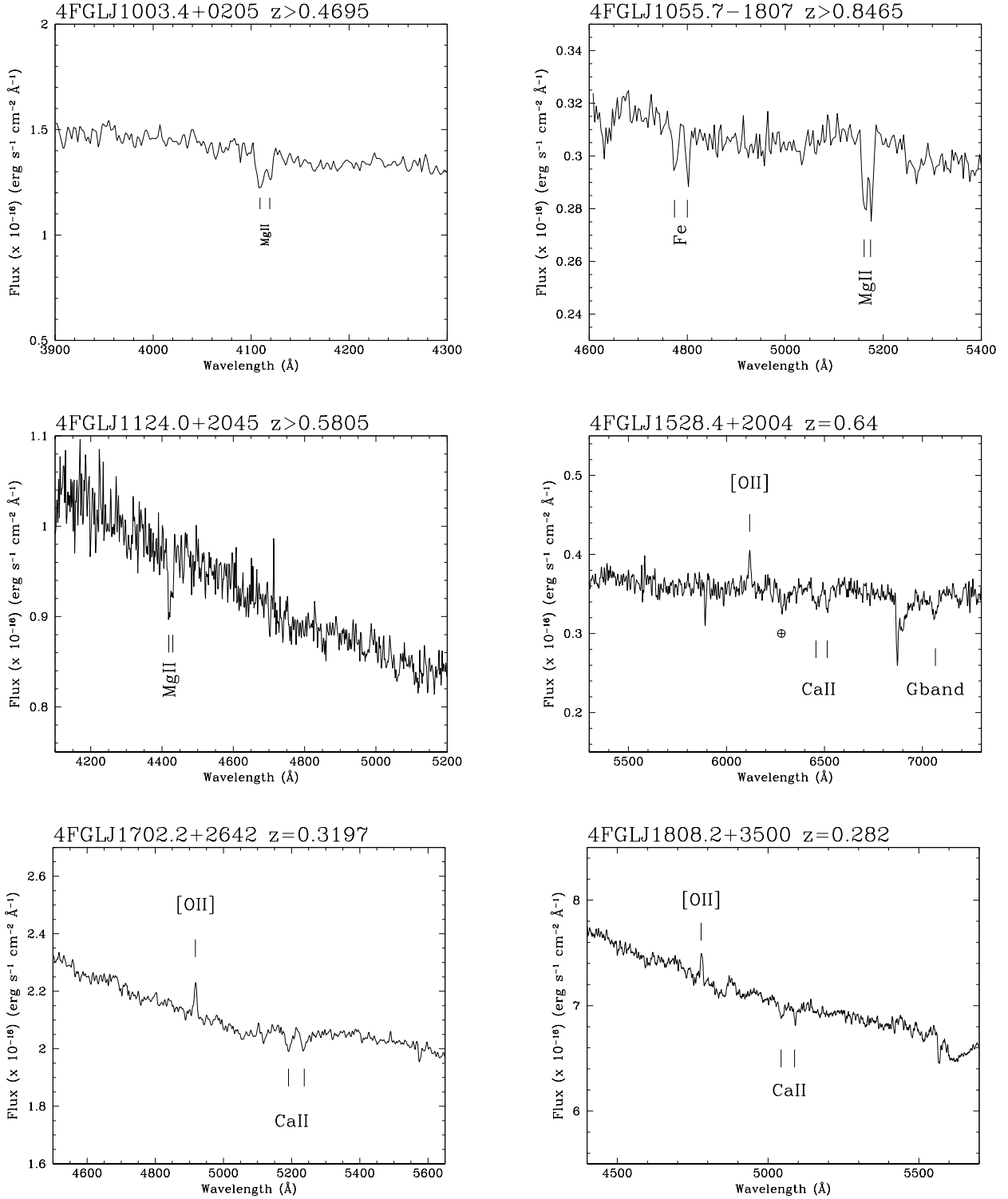


Figure A1. - Continued



**Figure A2.** Some examples of close-ups around the detected spectral lines of the spectra of the neutrino candidate blazars obtained at GTC, VLT and LBT. Main telluric bands are indicated by  $\oplus$ , spectral lines are marked by line identification.

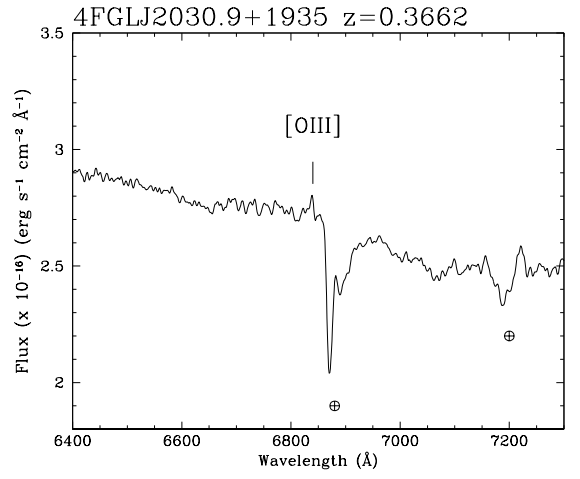
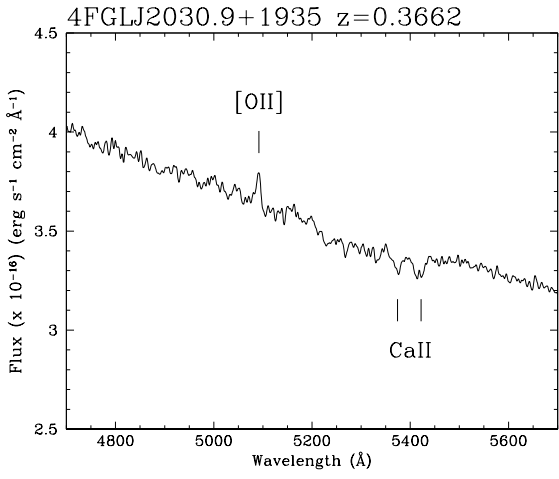
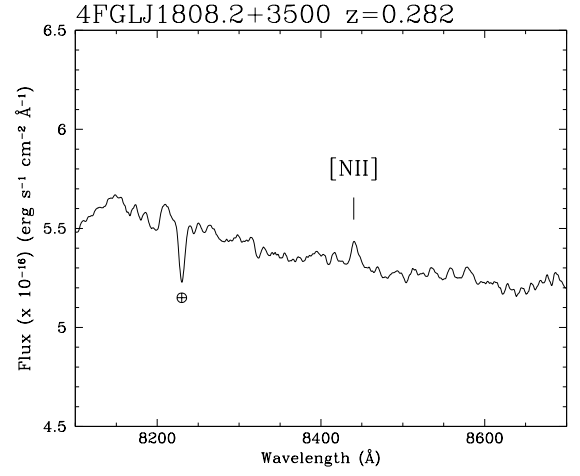
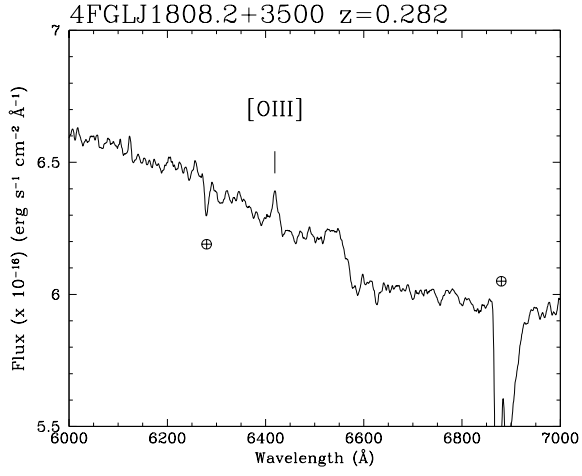
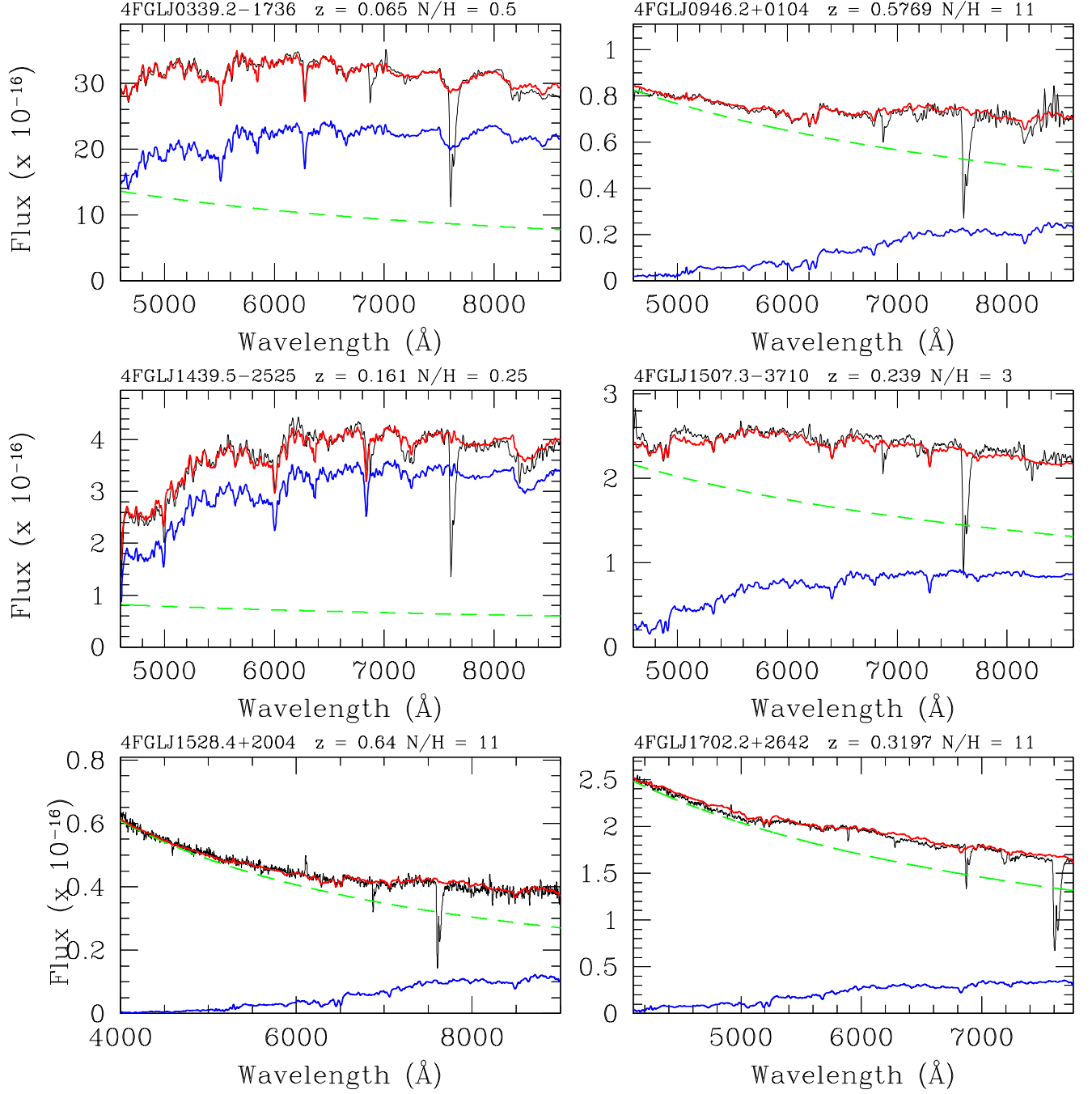


Figure A2. - Continued



**Figure A3.** Spectral decomposition of the observed optical spectrum (black line) of some targets of our sample into a power law (green dashed line) and an elliptical template for the host galaxy (blue line). The fit is given by the red solid line (see Section 4 for details). On each panel the nucleus to host ratio is given.



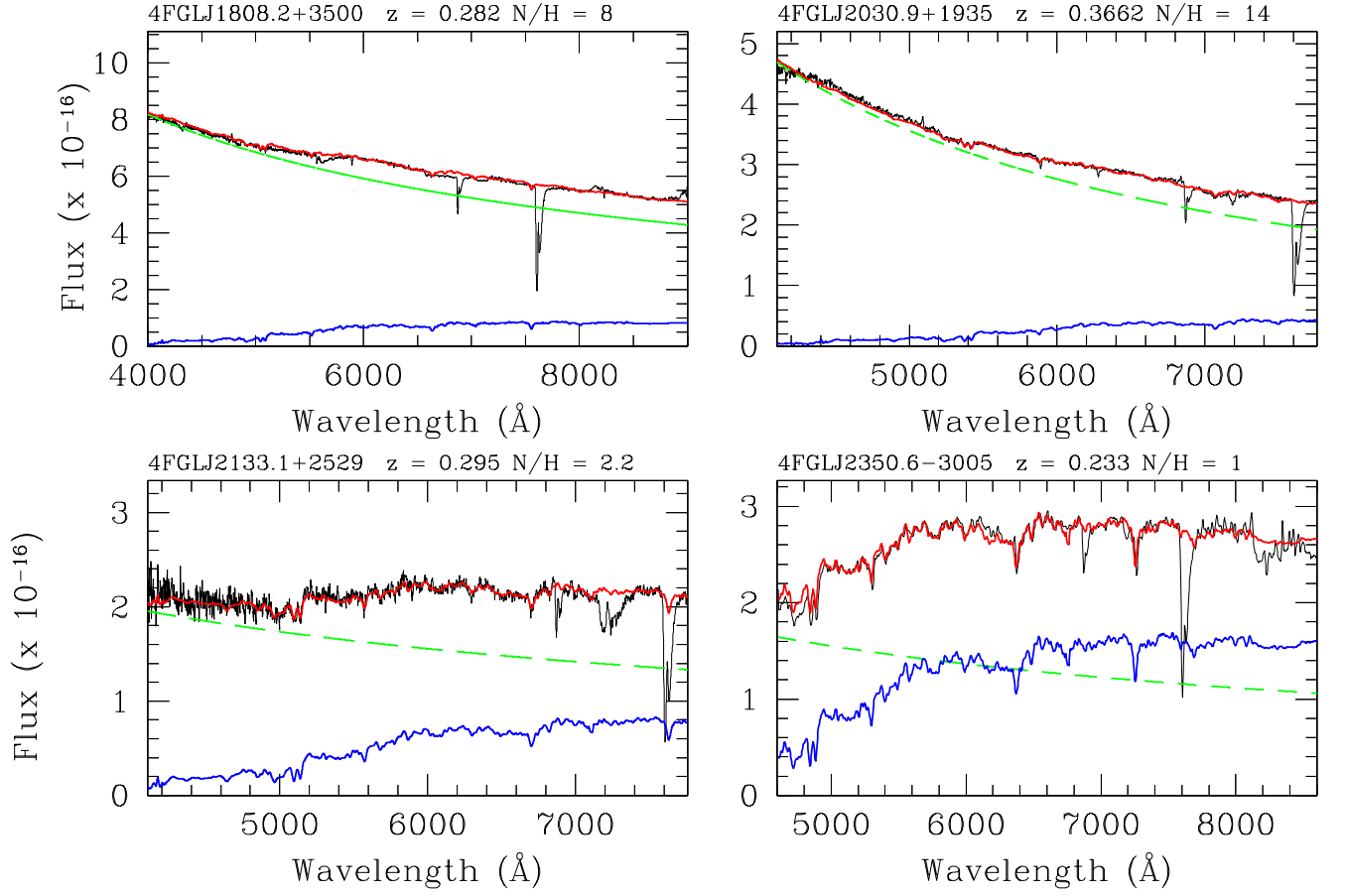


Figure A3. - Continued